Retinal isomerization in bacteriorhodopsin captured by a femtosecond X-ray laser

Przemyslaw Nogly[1], Tobias Weinert[1], Daniel James[1], Sergio Carbajo[2], Dmitry Ozerov[3], Antonia Furrer[1], Dardan Gashi[5], Veniamin Borin[4], Petr Skopintsev[1], Kathrin Jaeger[1], Karol Nass[5], Petra Båth[6], Robert Bosman[6], Jason Koglin[2], Matthew Seaberg[2], Thomas Lane[2], Demet Kekilli[1], Steffen Brünle[1], Tomoyuki Tanaka[7,10], Wenting Wu[1], Christopher Milne[5], Thomas White[8], Anton Barty[8], Uwe Weierstall[9], Valerie Panneels[1], Eriko Nango[7,10], So Iwata[7,10], Mark Hunter[2], Igor Schapiro[4], Gebhard Schertler[1,11], Richard Neutze[6], Jörg Standfuss[1,*]

[1] Division of Biology and Chemistry - Laboratory for Biomolecular Research, Paul Scherrer Institut, 5232 Villigen, Switzerland.

[2] Linac Coherent Light Source, Stanford Linear Accelerator Center (SLAC) National Accelerator Laboratory, 2575 Sand Hill Road, Menlo Park, CA 94025, USA.

[3] Science IT, Paul Scherrer Institut, 5232 Villigen, Switzerland.

[4] Fritz Haber Center for Molecular Dynamics, Institute of Chemistry, The Hebrew University of Jerusalem, Jerusalem 91904, Israel.

[5] SwissFEL, Paul Scherrer Institut, 5232 Villigen, Switzerland.

[6] Department of Chemistry and Molecular Biology, University of Gothenburg, Box 462, SE- 40530 Gothenburg, Sweden.

[7] RIKEN SPring-8 Center, 1-1-1 Kouto, Sayo-cho, Sayo-gun, Hyogo 679-5148, Japan.

[8] Center for Free-Electron Laser Science (CFEL), DESY, Notkestrasse 85, 22607 Hamburg, Germany.

[9] Department of Physics, Arizona State University, Tempe, AZ 85287, USA.

[10] Department of Cell Biology, Graduate School of Medicine, Kyoto University, Yoshidakonoe- cho, Sakyo-ku, Kyoto, 606-8501, Japan.

[11] Department of Biology, ETH Zurich, 8093 Zürich, Switzerland.

*Correspondence to: joerg.standfuss@psi.ch

One Sentence Summary: Ultrafast crystallography captures the photoresponse of retinal in bacteriorhodopsin

Ultrafast isomerization of retinal is the primary step in photoresponsive biological functions including vision in humans and ion-transport across bacterial membranes. We studied the sub-picosecond structural dynamics of retinal isomerization in the light-driven proton pump bacteriorhodopsin using an X-ray laser. A series of structural snapshots with near-atomic spatial and temporal resolution in the femtosecond regime show how the excited all-*trans* retinal samples conformational states within the protein binding pocket prior to passing through a twisted geometry and emerging in the 13-*cis* conformation. Our findings suggest ultrafast collective motions of aspartic acid residues and functional water molecules in the proximity of the retinal Schiff base as a key ingredient for this stereo-selective and efficient photochemical reaction.

Nature harvests light for its energy and information content. Seven-transmembrane helix retinal proteins use the absorption of photons to achieve both of these purposes across all domains of life. Family members include visual rhodopsins (light receptors triggering vision) in animals as well as bacteriorhodopsin and proteorhodopsins (proton pumps), halorhodopsins (anion pumps), channelrhodopsins (gated ion channels) and sensory rhodopsin (phototaxis receptors) in archaea and bacteria. Retinal-binding ion pumps and channels have found exciting applications in the optogenetic manipulation of neural cells (*1*). Activation of seven-transmembrane helix retinal proteins is initiated by the photochemical *trans-to-cis* (or *cis-to-trans* for visual rhodopsins) isomerization of the conjugated double bond system of the retinal chromophore. Photo-isomerization is one of the fastest reactions in biology being completed within a few picoseconds after photon absorption. Retinal isomerization occurs stereo-selectively at a specific double bond within the binding pocket of the protein host and with a quantum yield of up to 67% (*2*, *3*). This

contrasts with retinal in solution, for which illumination of all-*trans* retinal leads to formation of a mixture of different stereoisomers, 13-*cis*, 11-*cis* and 9-*cis*, with a quantum yield of only a few percent for each sub-product (*4*). How the protein scaffold rapidly guides retinal isomerization towards a single high-yield product is an outstanding and fundamental question in photobiology.

Bacteriorhodopsin (bR) is an archetypical proton pump that has long served as a system for understanding how the energy of a captured photon may be utilized to achieve unidirectional proton transport against a transmembrane proton concentration gradient. Chemical insights into retinal isomerization have emerged from ultrafast spectroscopy, which identified the I, J and K intermediates rising and decaying in the ultrafast time regime **(Figure 1)** (*5*–*8*). Hybrid quantum mechanics and molecular mechanics (QM/MM) simulations have provided further insight into the initial steps of retinal isomerization including predictions of energy and charge redistributions (*9*). Despite these advances, theoretical and spectroscopic studies require complementary structural information in order to build up a complete picture of the highly efficient photo-isomerization of retinal within proteins. X-ray structures have described reaction cycle intermediates after illuminating crystals with visible light or changing their pH (*10*). Such intermediate trapping studies, however, yielded conflicting results for the earliest available intermediate, i.e. K (*11*–*13*). Importantly, they cannot address the first events upon photo-isomerization since the low thermal energy barriers are not rate-limiting on the ultrafast time-scale.

With the advent of X-ray free electron lasers (XFELs), time-resolved serial femtosecond crystallography (TR-SFX) has emerged as a powerful method to study ultrafast structural changes in proteins (*14*). TR-SFX was validated against time-resolved Laue diffraction recorded at a

synchrotron radiation source using photoactive yellow protein (PYP) as a model system (*15*). The method has further provided unique insight into ultrafast structural changes during the photo-dissociation of carbon monoxide from the active site of myoglobin (*16*), isomerization of p-coumaric acid in PYP (*17*) and isomerization of hydroxybenzylidene imidazolinone in rsEGFP2 (*18*). TR-SFX has also tracked the evolution of protein and water molecule rearrangements within bR from nanoseconds to milliseconds from which a coherent picture of proton pumping emerged (*19*). Here we utilize this powerful new methodology to characterize the photo-isomerization of retinal and the immediate adaptations of its protein binding pocket.

X-ray diffraction data were collected to 1.50 Å resolution (**Table S1**) from a continuous stream of light adapted bR microcrystals grown in a lipidic cubic phase (LCP) (*20*, *21*) at the coherent X-ray imaging (CXI) beamline (*22*) of the Linac Coherent Light Source (LCLS) (*23*). Approximately one million indexable diffraction patterns were collected in a pump-probe scheme using a sequence of four X-ray probe pulses between every optical pump laser pulse (**Figure S1**) (*24*). The X-ray diffraction images immediately following the optical laser pulse at four nominal delays were sorted into sub-groups based on the LCLS timing tool signal (*25*) with a temporal resolution estimated to be in the order of 200 fs (*16*, *17*) (**Figure S2**). Sequential windows of data within the first picosecond (overlapping pump-probe delay (Δt) ranges with ~30000 sorted diffraction patterns) together with data collected at Δt=10 ps and Δt=8.33 ms yielded 20 snapshots of bR activation.

Trajectory of retinal isomerization

A long-distance overview of electron density changes (F_{obs}^{light} - F_{obs}^{dark}) within bR during the course of the first ten picoseconds is shown in **Movie S1**. Changes are already visible for the

earliest time-point and are initially clustered at the retinal and its binding pocket. A close-up view on the retinal chromophore (**Figure 2, Movie S2**) reveals negative density features that are visible above 4 σ (σ is the root mean square deviation of electron density) on the carbon atoms of the retinal polyene backbone (associated with C8, C10, C12 and C14) and corresponding weaker positive features (2.7-4.4 σ; see **Supporting Data File 1**) for $\Delta t \leq 500$ fs, but which decay for later time delays. Theoretical analyses have argued that photon absorption induces a partial charge relocation in retinal from the Schiff base (SB) towards the β-ionone ring in the excited state and prior to the *trans*-to-*cis* isomerization (*9*). Measurements of transient changes in the excitonic coupling between the retinal dipole moment and nearby tryptophan residues imply that this charge redistribution occurs within 200 fs after photon absorption (*5*). Simultaneously, nuclear rearrangements lead to an extension of double bonds and contraction of the single bonds (so called inversion of the bond length alternation), which allows the planar geometry of retinal to distort in the excited state (*26*). Such distortion is consistent with the negative and (weaker) positive difference Fourier electron density map (F_{obs}^{light} - F_{obs}^{dark})features observed around the C7 to C14 atoms of the retinal (**Figure 2**) on this time-scale.

The retinal initially samples possible isomerization geometries for $\Delta t \leq 500$ fs but the possible evolution is heavily constrained by the rigidity of the binding pocket. Following this sampling of double bond geometries in the initial excited state, electron density changes focus around the C13=C14 double bond suggesting a coordinated evolution throughout the *trans-cis* isomerization. The progress of retinal isomerization can be followed in extrapolated electron density maps (**Figure S3, Movie 1**). Changes over time are best visualized by overlaying the difference Fourier electron density map (F_{obs}^{light} - F_{obs}^{dark}) with the resting and refined structures for the time ranges Δt = 49 to 406 fs; 457 to 646 fs; 10 ps; and 8.33 ms (**Table S2**) with (**Figure 3**). These time-

windows correlate approximately with accumulation of the spectroscopically distinct I, J, K and M intermediates identified in solution (*5–8*, *27*, *28*). Already for the earliest temporal windows paired difference density features indicate that the retinal Schiff base nitrogen is displaced towards helix G, which is quantified by structural refinement as a 0.5 Å sideways-motion of the SB but with the retinal geometry otherwise remaining rather similar to the all-*trans* conformation. For Δt = 457 to 646 fs, we observe stronger continuous negative difference Fourier electron density map (F_{obs}^{light} - F_{obs}^{dark}) along the C20-C14=C13 bonds and two positive difference density peaks flank a negative feature on the SB nitrogen. This time-point is modeled as a twisted retinal configuration with the C12-C13=C14-C15 torsion angle approximately 90° and the C15=Nζ bond lying in the plane of the membrane. Overall changes between the dark and Δt = 457 to 646 fs time delay twist the torsion angles of the C13=C14 and the neighboring C11=C12 and C15=Nζ bonds in opposite directions, indicating that the reaction proceeds according to the aborted bicycle-pedal model of retinal isomerization (*9*, *29*, *30*).

By Δt = 10 ps only one positive difference Fourier electron density map (F_{obs}^{light} - F_{obs}^{dark}) feature remains that is complementary to the negative peak on the SB nitrogen atom and paired positive and negative density features are associated with the retinal C20 methyl group. Structural refinement captures these changes as the retinal having reached its twisted 13-*cis* configuration and the C20 methyl being twisted towards helix G. This sequence of events is entirely consistent with quantum mechanical and molecular mechanical (QM/MM) simulations of the retinal excited state when the key Wat402, Lys216 and the counter-ion network are included within the modeled domain (**Figure S4** and Altoè *et al*. (*9*)) providing theoretical support for the structural evolution observed here. Finally, the difference Fourier electron density map recorded for Δt = 8.33 ms

displays all major features previously observed for Δt = 1.725 ms (*19*) including the planar 13-*cis* retinal characteristic of later reaction intermediates of the bR photocycle.

Ultrafast response of the counter-ion cluster

A key feature in the resting bR state is a hydrogen bond (H-bond) interaction of the SB with Wat402, which participates in the hydrogen bonding network with the counter-ions Asp85 and Asp212 and stabilizes the positive charge on the SB nitrogen (*31*). Mutation of either Asp85 or Asp212 to non-charged residues greatly reduces the rate of retinal isomerization (*32*) and both have been implicated in guiding stereoselectivity of the reaction (*33*).

Quite remarkably, Wat402 and the SB respond to the photon absorption of retinal even before the isomerization appears to begin, moving up to 0.6 Å further away from each other (to a distance of 3.25 Å) following light absorption (Δt = 49 to 406 fs). This separation increases to 4.05 Å once the retinal is isomerized (Δt = 10 ps). This movement is visualized as very strong paired positive and negative difference Fourier electron density map (F_{obs}^{light} - F_{obs}^{dark}) features (from 6 σ to 11 σ, **Figure 4)** associated with Wat402, Asp212 and Tyr57 and which together reveal an ultrafast collective motion of a group of polar residues connected through H-bond interactions (**Movie 2)**. The driving force for this motion is the ultrafast redistribution of the positive charge away from the SB and towards the β-ionone ring. Quantum chemical calculation of the difference between the ground and excited state electron density (**Figure S4**) show the localization of changes along the retinal polyene chain. The sudden polarization instantaneously pushes the water molecule away from the SB (up to a distance of 3.65 Å at Δt= 457 to 646 fs) and breaks the SB-Wat402 H-bond (which would otherwise oppose the SB reorientation during isomerization). Loss of the H-bond lowers the energy barrier for a specific isomerization pathway (*34*) allowing the retinal to

isomerize about the C13=C14 bond. These collective motions are later damped with the retinal being fully isomerized at Δt = 10 ps while Wat402 loses its interaction to the SB in agreement with a changing hydrogen bonding pattern in this region predicted by low temperature Fourier transform infrared (*35*) and Raman spectroscopy (*36*). Overall it is striking that the rigidity of the large hydrophobic region of retinal binding pocket, which prevents unwanted C7=C8, C9=C10 or C11=12 *cis* products, is in stark contrast with the specific ultrafast motions associated with Wat402 and the counter-ion cluster. These findings implicate ultrafast collective motions as a key ingredient essential for efficient isomerization within the protein scaffold.

Protein quake

The collective motions from the counter-ion region extend up to 12 Å away from the SB nitrogen within 600 fs (**Figure S5**) yet become dispersed on longer time-scales. This dampening is evidenced by weaker paired difference densities associated with Tyr57 at Δt = 759-1025 fs, as well as the motions of Thr47, Asp212, which are no longer visible at Δt = 10 ps. Changes are further apparent when comparing the refined structural intermediates at Δt = 49 to 406 fs; 457 to 646 fs; and 10 ps (**Movie 2**). As such these motions propagate away from the active site at 2 nm/ps which is noticeably faster than the speed of sound in water (~1.5 nm/ps). These observations are consistent with the propagation of motions in the bacterial photoreaction center (*37*) and myoglobin (*16*, *38*, *39*) and the theory of protein quakes that suggests how excess energy in proteins can be dissipated in earthquake like motions of collective structural deformations (*40*). In the case of photoactive proteins like bR, these motions may be the mechanism through which excess energy from decay of the excited state is released in a non-radiative fashion.

Our ultrafast TR-SFX data recorded at an XFEL captures a fundamental photochemical reaction and one of the fastest processes in biology. In particular, our measurements uncover the initial structural rearrangements in the excited state that guide the selective isomerization process. Photo-excited retinal initially samples multiple isomerization pathways within its binding pocket, but the ultimate fate of the reaction is steered by the near instantaneous charge redistribution along the retinal and the resulting collective motions of the Schiff base counter-ion complex. Breaking of the SB-Wat402 H-bond enables the *trans*-to-*cis* isomerization about the C13=C14 double bond. Similar ultrafast collective motions may guide the stereochemistry and enhance the quantum efficiency of retinal isomerization in such diverse processes as phototrophy in the seas, neuron stimulation in optogenetics and the initiation of visual signals within the photo-receptors of our eyes.

Materials and Methods

Purification and Crystallization of bR

Bacteriorhodopsin was purified from purple membranes of *Halobacterium salinarum*. The purification and crystallization was performed as described previously (*24*, *41*) with a few modifications. The purple membranes were solubilized overnight in the presence of 1.7% β-Octylglucoside (Anatrace) and 50 mM sodium phosphate buffer pH 6.9 (GERBU). After solubilization the pH was adjusted to 5.5 with 0.1 M HCl and the insoluble fraction was removed by 1-hour centrifugation at 150 000 x g. The size exclusion purification step was omitted following Nango *et al*. (*19*). The protein was concentrated to 40 – 80 mg ml^{-1} using Millipore centricolumns with 50 kDa cutoff. Lipidic Cubic Phase (LCP) for crystallization was obtained in a Hamilton syringe by mixing protein with monoolein (Nu-Chek) in a 42:58 ratio. Subsequently the LCP was

slowly injected into another Hamilton syringe filled with crystallization buffer consisting of 100 mM Sorensen buffer pH 5.6 (GERBU) and 30% polyethylene glycol 2000 (Molecular Dimensions). The crystallization was carried out at 21°C and crystals between 15 µm and 50 µm along the longest edge and with a thickness of 1 – 5 µm were obtained within 3-6 days (average crystals size 35x35x3 µm). All purification and crystallization steps were performed under dim red light or in the dark.

Sample preparation for LCP-SFX

The crystallization buffer was removed from LCP containing crystals via a syringe coupler by slow pressing on the syringe plunger. Shortly before the experiment monoolein was added to bring the sample into a homogeneous and transparent LCP mesophase. The sample was supplemented with 5% of MAG 7.9 to prevent phase transition during injection into vacuum and 5% of paraffin was added to support smooth flow of the sample. The crystal density within the sample was homogenized using a custom made "3-way syringe coupler". It consisted of three syringe inlets and the simultaneous passage of sample from two syringes into a third one over several cycles ensured optimal crystal distribution throughout the sample volume for smooth jet operation. The stability of jetting was tested offline with a high-speed camera providing further evidence that the addition of paraffin improved stable jetting. Selected batches of the prepared crystalline sample were tested in advance to confirm high hit rates and diffraction quality using the Swiss Light Source set up for LCP injection (*42*). Before data collection the sample was light adapted at 300 mW for 5 minutes through a long-pass yellow filter (>515 nm). Sample was used for data collection no longer than 30 min after light exposure to prevent decay of the light adapted dark state. On average, 1 ml of final sample was used per 12-hour shift.

Data collection

The TR-SFX experiment was performed in June 2017 in the microfocus chamber of the CXI beamline at LCLS (*43*) with the integrated optical pump-probe laser set-up (*44*). The 50 fs XFEL pulses at 9.5 keV were delivered at 120 Hz into a vacuum chamber. In the experiment we used a modified version of the LCP injector (*20*) with a larger sample reservoir of 130 µl to allow a longer data collection and the higher flow rates (2.5 µl min^{-1} through a 50 µm diameter nozzle and, for a small amount of data, 5 µl min^{-1} through a 75 µm diameter nozzle) necessary for time-resolved crystallography (*24*). The LCP stream was aligned with the X-ray beam and an optical laser (Ti:Sapphire-pump Optical Parametric Amplifier, 30 Hz repetition rate, 100 fs pulse length, 17 µJ energy in a focal spot of 95 µm ($1/e^2$) at 529 nm wavelength. The arrival time of the optical laser pulse relative to the XFEL pulse, was monitored using the timing tool at LCLS (*25*, *45*) with nominal time delays Δt = -500 fs, 300 fs, 600 fs, 900 fs, 1100 fs and 10 ps. As the exact timing is subject to jitter, data collected at these delays were sorted and binned after collection based on their timing tool signal (see Data sorting and binning). By combining all indexed patterns from the second XFEL pulse after the pump laser excitation (175 µm from the interaction region) we could further resolve Δt = 8.33 ms, but with lower occupancy due to this time-point being excited further from the pump laser peak intensity (**Figure S1**). We obtained a high quality dark dataset (**Table S1**) by merging patterns of the fourth XFEL pulse after light excitation from all datasets. For clarity, the 120 Hz XFEL, 30 Hz optical data collection scheme is further illustrated in **Figure S1**. An important parameter for a successful TR-SFX experiment is the laser power density at sample position, which is critical for efficient activation but difficult to estimate. In our case we aligned the laser approximately 50 µm below the X-ray interaction region to exclude light contamination

of the following pulses. This shift reduced the nominal power density of 2.4 TW/cm^2 the laser to 0.324 TW/cm2 (factor of 0.135 (1/e^{-2})) at the X-ray interaction region. This value is in a similar range as in previously published ultrafast TR-SFX studies (16, 17, 46). Using an offline setup with a continuous laser we established that scattering from the 50 µm wide LCP jet (without protein or crystals) reduces the incident laser light by a factor of about 0.8. Scattering from the LCP jet and the high optical density further reduced the average light intensity any given bR molecule was exposed to. Taking the typical crystal dimensions of 35x35x3 µm^3 and optical density of crystals into account this corresponds to 3.3 to 0.6 absorbed photons per retinal depending on the orientation of the crystal. This is within the range where multiphoton effects are negligible in a crystallographic analysis based on the small spectroscopic effect under similar laser conditions (*46–48*). Moreover, our setup provided comparable results to our previous experiment using a nanosecond pump laser with much lower power density (0.06 GW cm^{-2}) at SACLA (*19*), with a twisted retinal at 10 ps and 16 ns (**Figure S7)**. The two delays correspond to the lower and upper end of the temporal range where the K intermediate of bR is observed spectroscopically and the high similarity between the two structures indicates that productive photocycles can be induced using a femtosecond laser pump pulse. The similarity of structures for 10 ps / 16 ns provides us with an internal control for the presented experiments in the femtosecond range.

Our choice of laser energy was guided by two previous TR-SFX experiments with very similar femtosecond pump laser parameters but different laser energies (**Figure S9**). In December 2015, we used 8 µJ and 12 µJ, with the former yielding nearly flat Fourier difference electron density maps while the latter provided very weak signal with a few peaks at 3.5 σ and the estimated activation levels of about 5%. In July 2014, we used 20 µJ which yielded about 13% activation levels (*24*). In the currently reported experiment we aimed for activation levels better than 10%

and measured all time-delays with a consistent 17 μJ in order to obtain interpretable crystallographic data.

Data sorting and binning

Diffraction images were selected with Cheetah (*49*) followed by further sorting according to event codes corresponding to one of the four images collected after the optical laser pulse.

Light data in the femtosecond range were sorted by pump-probe delay time using the timing tool available at CXI with yttrium aluminum garnet (YAG) target (*45*). The spectrally encoded delay was determined by the standard matched-filter procedure implemented in psana, the LCLS-provided analysis software (*50*). Strong etalon effects caused by the thick YAG target necessitated one modification to this standard analysis. Before edge-position determination by matched filtering, the spectral signal was bandstop filtered using a 5th-order Butterworth filter with a cut-on and cut-off frequency of 45 fs^{-1} and 120 fs^{-1} respectively, effectively removing signal oscillations due to etalon. The data where initially sorted into 20 bins with 10000 images each (see **Figure S1**). For calculating structural snapshots, we combined 3 overlapping bins which lead to 18 snapshots in the femtosecond range, which we further complement with data collected at Δt =10 ps and 8.33 ms (**see Table S1**).

Data processing

The images were indexed using mosflm and dirax indexing algorithms on the peaks identified by Cheetah. Data were integrated (the integration radius was 3 pixels for the peak region and 4-7 pixels for the background annulus with integrating 1.2 nm^{-1} beyond the conservative resolution limit determined on a per image basis) and merged with CrystFEL (*51*) version 0.6.3. A geometry

refinement using geoptimiser was carried out on a subset of images that diffracted beyond 2.0 Å in CrystFEL's conservative apparent resolution. This step improved high resolution statistics significantly after re-indexing and re-integration of the data. The indexing ambiguity in space group $P6_3$ was resolved using ambigator in CrystFEL (*52*). Data were scaled and merged using partialator in CrystFEL without the calculation of partialities (--model = unity), using one cycle of scaling and applying the option to extend the conservative resolution limit determined on the per image basis ("--pushres 1.2"). A small subset of patterns (11758) with HPLC back pressures 25 bars above the average value for each data run was discarded in order to eliminate any source of potential light contamination in dark data due to occasional jet slowdowns owing to higher crystal density.

Data analysis

For the structure determination of the dark state, diffraction images from every fourth diffraction image after the optical laser pulse were used. The signal recorded by the timing tool for every first diffraction image after the optical laser pulse was used to sort the diffraction images after the experiment into bins with defined time ranges (see Data processing and binning). Each of the datasets (**Table S1**) consists of three overlapping original bins (**Figure S1**). The time ranges used for data analysis were initially chosen to contain around 30000 images (about 27000 after indexing, see **Table S1**) to ensure good quality data for analysis and to be comparable to the number of images collected at 10 ps. The resolution cutoff for the light data was established so that most datasets have at least a CC* of 0.5 at 1.50 Å. We used a dark dataset of 29461 patterns collected without optical pump laser to cross-check our high quality dark dataset for light contamination and

could not observe difference density peaks corresponding to the M-state above the noise level of 2.5 σ.

Structure determination and refinement of the bR dark state

PDB entry with accession code 5J7A (*24*) with all water molecules and lipids removed was used as molecular replacement model in Phaser (*53*). The resting state structure was obtained with several cycles of building and refinement using COOT (*54*) and PHENIX (*55*) to a resolution of 1.5 Å (**Table S2**).

Calculation of difference Fourier density maps

The difference Fourier density maps were calculated with phenix.fobs_minus_fobs_map (*55*) including the multiscaling feature and low resolution cutoff at 4.5 Å. The electron density peak minima and maxima in σ units (= root mean square electron density of the unit cell) were extracted in COOT (*56*). **Supporting Data File 1** lists peak values for regions of the density map which at any point in the ultrafast time range exceeded +/- 4 σ. The values below 2.5 σ were set to 0 as being of too low significance.

Refinement of intermediate states

In a TR-SFX experiment crystals subjected to optical laser light pulse contain a mixture containing light activated molecules and dark state molecules. We used extrapolated structure factors F_{ext} (*57*) to enable modeling of bacteriorhodopsin activated states, similar approach as used to model the subpicosecond structural states of PYP (*17*). The extrapolated structure factors were calculated using a linear approximation (*58*) as follows: $F_{ext} = [(F_{obs\_light} - F_{obs\_dark}) / \text{activated fraction}] +$

F_{obs_dark}. The $2F_{ext}$ - F_{calc} maps calculated with phases of the dark state model showed distinct features in agreement with the F_{obs}^{light} - F_{obs}^{dark} Fourier difference maps. Using this comparison, the light activated fraction of molecules in the data time-ranges 49 - 406 fs, 457 - 646 fs, 10 ps, 8.3 ms was estimated to be 25 %, 18 %, 16 % and 10 % corresponding to fractions where the features associated exclusively with the dark state disappear from extrapolated maps. Reciprocal space refinement against the F_{ext} to 1.9 Å resolution in PHENIX (*55*) in combination with real space fitting in COOT (*56*) provided models (**Table S2**) for the respective time points with all of them showing about 98% of residues in the Ramachandran favored region. A comparison of calculated ($F_{calc}^{refined}$ - F_{calc}^{dark}) and experimental (F_{obs}^{light} - F_{obs}^{dark}) difference densities (**Figure S8**) was used as additional control to validate the refined structures. Comparison of the bR 8.33 ms structure obtained from the refinement against the extrapolated structure factors with the 1.725 ms structure (*19*) obtained by an alternative conformation refinement approach shows a high level of similarity between the structures derived using the two different approaches (**Figure S6**).

Quantum mechanics and molecular mechanics (QM/MM) calculations

We used a hybrid quantum mechanics/molecular mechanics (QM/MM) method to study the photochemical reaction of bR. The key step in setting up such a QM/MM calculation is the partitioning of the total system in the QM and MM subsystems. The QM subsystem is described using a quantum chemical method, while the MM subsystem is computed by a classical force field. Following the crystallographic results, we included the retinal chromophore and the Lys216 sidechain, as well as the counter-ion sidechains Arg82, Asp85, Asp212 and the water molecules Wat402, Wat404, Wat406 to the QM part, while the rest of the protein was treated at the MM level. The MM subsystem is treated using an AMBER force field and interacts with the QM

subsection through electrostatic embedding. In all the simulations we have performed the protein backbone was kept fixed in the crystallographic position and only the QM section and all sidechains, which have at least one atom within 5 Å from the retinal Schiff base and Lys216 moiety was allowed to be moved freely in the geometry optimization.

To optimize the geometry in the ground state the QM subsystem was described using the pure-GGA BP86 functional with Grimme's corrections for dispersion interactions and the cc-pVDZ basis set. The difference between the ground and excited state density was computed using CAM-B3LYP and the cc-pVTZ basis set.

Acknowledgements

We thank SwissFEL and particularly Rafael Abela for their constant logistic and financial support in implementing injector-based serial crystallography. We thank Florian Dworkowski for help with auxiliary LCP absorption and scattering experiments. We are grateful to the staff at the X06SA beamline at the Swiss Light Source for their assistance in pretesting crystals. Data collection was carried out at the Linac Coherent Light Source (LCLS) at the SLAC National Accelerator Laboratory during the LP41 beamtime in June 2017.

Funding

Use of the Linac Coherent Light Source (LCLS), SLAC National Accelerator Laboratory, is supported by the U.S. Department of Energy, Office of Science, Office of Basic Energy Sciences under Contract No. DE-AC02-76SF00515. T.T., E.N., and S.I. acknowledge support from the X-ray Free Electron Laser Priority Strategy Program (MEXT) and the Platform Project for Supporting Drug Discovery and Life Science Research from Japan Agency for Medical Research

and Development. Th.W and A.B. acknowledge funding from the Helmholtz Association via Programme Oriented Funds. I.S. has received funding from the European Research Council (ERC) under the European Union's Horizon 2020 research and innovation program (grant agreement 678169 "PhotoMutant").

The work was financially supported by the grants FP7-PEOPLE-2011-ITN 317079 NanoMem (to G.S. and R.N.) and Horizon2020 grant XPROBE 637295 (to R.N). We further acknowledge the Swiss National Science Foundation for grants 310030_153145 (to G.S.), PZ00P3_174169 (to P.N.) and 31003A_159558 (to J.S.). P.N. acknowledges support from the European Community's Seventh Framework Program (FP7/2007-2013) under grant agreement n.°290605 (PSI-FELLOW/COFUND). We acknowledge support from the Data Analysis Service (142-004) project of the Swiss Universities SUC-P2 program. R.N. acknowledges funding from the Swedish Research Council (2015–00560 and 349-2011-6485), the Swedish Foundation for Strategic Research (SRL10-0036), the Knut and Alice Wallenberg Foundation (KAW 2014.0275).

Author contributions

P.N., T.W., and J.S. conceived the research with suggestions on pump-probe experiments from C.M. and ultrafast biology from R.N.. P.N., A.F., W.W., K.J., and V.P. prepared protein and microcrystals. P.N., A.F., K.J. and P.B. prepared sample during data collection. Crystal injection was optimized by P.N. and D.J.. The lipidic cubic phase injector with large reservoir was designed by U.W. and operated by D.J., D.G. and P.S. during data collection. Data processing during the beamtime was done by T.W., D.O., K.N. and A.B. implementing suggestions from Th.W. Final sorting of data in the femtosecond domain was done by T.W., D.O., A.B. using code developed by T.L.. Progress during the beamtime was recorded by V.P. and R.B.. The probe laser was

installed and aligned by S.G.. The CXI endstation was controlled by M.H., J.K. and M.S. during the beamtime. QM/MM simulations were contributed from V.B. and I.S. Post-beamtime serial data processing, data analysis and structural refinement were done by P.N. and T.W.. D.K, S.B. and C.W. assisted with data interpretation. S.I. and G.S. supported the project. M.H. was coordinating efforts at the LCLS, E.N. at SACLA, I.S. at the UJ, R.N. at the UG and J.S. at the PSI. The manuscript was written by R.N., P.N. and J.S. with direct contributions from most authors. All authors read and acknowledged the manuscript.

Competing interests

The authors declare to have no competing interests.

Data and material availability

Coordinates and structure factors have been deposited in the PDB database under accession codes 6G7H (dark state), 6G7I (Δt=49-406 fs), 6G7J (Δt= 457-646 fs), 6G7K (Δt=10 ps), and 6G7L (Δt=8.33 ms). Scripts used for correcting the jitter in the sub-picosecond time delays are available upon request to Thomas Lane Stanford Linear Accelerator Center (SLAC) National Accelerator Laboratory. Other software used for data evaluation is freely available as detailed in the material and methods section.

REFERENCES

1. B. R. Rost, F. Schneider-Warme, D. Schmitz, P. Hegemann, Optogenetic Tools for Subcellular Applications in Neuroscience. *Neuron*. **96**, 572–603 (2017).

2. P. Hamm *et al.*, Femtosecond spectroscopy of the photoisomerisation of the protonated Schiff base of all-trans retinal. *Chem. Phys. Lett.* **263**, 613–621 (1996).

3. O. P. Ernst *et al.*, Microbial and Animal Rhodopsins: Structures, Functions, and Molecular Mechanisms. *Chem. Rev.* **114**, 126–163 (2014).

4. K. A. Freedman, R. S. Becker, Comparative investigation of the photoisomerization of the protonated and unprotonated n-butylamine Schiff bases of 9-cis-, 11-cis-, 13-cis-, and all-trans-retinals. *J. Am. Chem. Soc.* **108**, 1245–1251 (1986).

5. S. Schenkl, F. van Mourik, G. van der Zwan, S. Haacke, M. Chergui, Probing the Ultrafast Charge Translocation of Photoexcited Retinal in Bacteriorhodopsin. *Science*. **309**, 917–920 (2005).

6. T. Kobayashi, T. Saito, H. Ohtani, Real-time spectroscopy of transition states in bacteriorhodopsin during retinal isomerization. *Nature*. **414**, 35107042 (2001).

7. J. Herbst, K. Heyne, R. Diller, Femtosecond infrared spectroscopy of bacteriorhodopsin chromophore isomerization. *Science*. **297**, 822–825 (2002).

8. G. H. Atkinson, T. L. Brack, D. Blanchard, G. Rumbles, Picosecond time-resolved resonance Raman spectroscopy of the initial trans to cis isomerization in the bacteriorhodopsin photocycle. *Chem. Phys.* **131**, 1–15 (1989).

9. P. Altoè, A. Cembran, M. Olivucci, M. Garavelli, Aborted double bicycle-pedal isomerization with hydrogen bond breaking is the primary event of bacteriorhodopsin proton pumping. *Proc. Natl. Acad. Sci.* **107**, 20172–20177 (2010).

10. C. Wickstrand, R. Dods, A. Royant, R. Neutze, Bacteriorhodopsin: Would the real structural intermediates please stand up? *Biochim. Biophys. Acta*. **1850**, 536–553 (2015).

11. K. Edman *et al.*, High-resolution X-ray structure of an early intermediate in the bacteriorhodopsin photocycle. *Nature*. **401**, 822–826 (1999).

12. B. Schobert, J. Cupp-Vickery, V. Hornak, S. O. Smith, J. K. Lanyi, Crystallographic Structure of the K Intermediate of Bacteriorhodopsin: Conservation of Free Energy after Photoisomerization of the Retinal. *J. Mol. Biol.* **321**, 715–726 (2002).

13. Y. Matsui *et al.*, Specific Damage Induced by X-ray Radiation and Structural Changes in the Primary Photoreaction of Bacteriorhodopsin. *J. Mol. Biol.* **324**, 469–481 (2002).

14. R. Neutze, K. Moffat, Time-resolved structural studies at synchrotrons and X-ray free electron lasers: opportunities and challenges. *Curr. Opin. Struct. Biol.* **22**, 651–659 (2012).

15. J. Tenboer *et al.*, Time-resolved serial crystallography captures high-resolution intermediates of photoactive yellow protein. *Science*. **346**, 1242–1246 (2014).

16. T. R. M. Barends *et al.*, Direct observation of ultrafast collective motions in CO myoglobin upon ligand dissociation. *Science*. **350**, 445–450 (2015).

17. K. Pande *et al.*, Femtosecond structural dynamics drives the trans/cis isomerization in photoactive yellow protein. *Science*. **352**, 725–729 (2016).

18. N. Coquelle *et al.*, Chromophore twisting in the excited state of a photoswitchable fluorescent protein captured by time-resolved serial femtosecond crystallography. *Nat. Chem.* **10**, 31–37 (2018).

19. E. Nango *et al.*, A three-dimensional movie of structural changes in bacteriorhodopsin. *Science*. **354**, 1552–1557 (2016).

20. U. Weierstall *et al.*, Lipidic cubic phase injector facilitates membrane protein serial femtosecond crystallography. *Nat. Commun.* **5** (2014), doi:10.1038/ncomms4309.

21. E. M. Landau, J. P. Rosenbusch, Lipidic cubic phases: a novel concept for the crystallization of membrane proteins. *Proc. Natl. Acad. Sci. U. S. A.* **93**, 14532–14535 (1996).

22. S. Boutet, G. J. Williams, The Coherent X-ray Imaging (CXI) instrument at the Linac Coherent Light Source (LCLS). *New J. Phys.* **12**, 035024 (2010).

23. P. Emma *et al.*, First lasing and operation of an ångstrom-wavelength free-electron laser. *Nat. Photonics*. **4**, 641–647 (2010).

24. P. Nogly *et al.*, Lipidic cubic phase injector is a viable crystal delivery system for time-resolved serial crystallography. *Nat. Commun.* **7**, 12314 (2016).

25. M. Harmand *et al.*, Achieving few-femtosecond time-sorting at hard X-ray free-electron lasers. *Nat. Photonics*. **7**, 215–218 (2013).

26. R. González-Luque *et al.*, Computational evidence in favor of a two-state, two-mode model of the retinal chromophore photoisomerization. *Proc. Natl. Acad. Sci.* **97**, 9379–9384 (2000).

27. S. Schenkl *et al.*, Insights into excited-state and isomerization dynamics of bacteriorhodopsin from ultrafast transient UV absorption. *Proc. Natl. Acad. Sci. U. S. A.* **103**, 4101–4106 (2006).

28. G. H. Atkinson, L. Ujj, Y. Zhou, Vibrational Spectrum of the J-625 Intermediate in the Room Temperature Bacteriorhodopsin Photocycle. *J. Phys. Chem. A*. **104**, 4130–4139 (2000).

29. A. Warshel, Bicycle-pedal model for the first step in the vision process. *Nature*. **260**, 679–683 (1976).

30. A. Warshel, Z. T. Chu, Nature of the Surface Crossing Process in Bacteriorhodopsin: Computer Simulations of the Quantum Dynamics of the Primary Photochemical Event. *J. Phys. Chem. B*. **105**, 9857–9871 (2001).

31. M. Sheves, N. Friedman, A. Albeck, M. Ottolenghi, Primary photochemical event in bacteriorhodopsin: study with artificial pigments. *Biochemistry (Mosc.)*. **24**, 1260–1265 (1985).

32. L. Song, M. A. El-Sayed, J. K. Lanyi, Protein Catalysis of the Retinal Subpicosecond Photoisomerization in the Primary Process of Bacteriorhodopsin Photosynthesis. *Science*. **261**, 891–894 (1993).

33. T. Yamato, T. Kakitani, Molecular Dynamics Simulation of the Excited-State Dynamics of Bacteriorhodopsin. *Photochem. Photobiol.* **66**, 735–740 (1997).

34. F. Gai, K. C. Hasson, J. C. McDonald, P. A. Anfinrud, Chemical Dynamics in Proteins: The Photoisomerization of Retinal in Bacteriorhodopsin. *Science*. **279**, 1886–1891 (1998).

35. M. Shibata, H. Kandori, FTIR studies of internal water molecules in the Schiff base region of bacteriorhodopsin. *Biochemistry (Mosc.)*. **44**, 7406–7413 (2005).

36. S. Shim, J. Dasgupta, R. A. Mathies, Femtosecond Time-Resolved Stimulated Raman Reveals the Birth of Bacteriorhodopsin's J and K Intermediates. *J. Am. Chem. Soc.* **131**, 7592–7597 (2009).

37. D. Arnlund *et al.*, Visualizing a protein quake with time-resolved X-ray scattering at a free-electron laser. *Nat. Methods*. **11**, 923–926 (2014).

38. L. U. L. Brinkmann, J. S. Hub, Ultrafast anisotropic protein quake propagation after CO photodissociation in myoglobin. *Proc. Natl. Acad. Sci.* **113**, 10565–10570 (2016).

39. M. Levantino *et al.*, Ultrafast myoglobin structural dynamics observed with an X-ray free-electron laser. *Nat. Commun.* **6**, 6772 (2015).

40. A. Ansari *et al.*, Protein states and proteinquakes. *Proc. Natl. Acad. Sci. U. S. A.* **82**, 5000–5004 (1985).

41. P. Nogly *et al.*, Lipidic cubic phase serial millisecond crystallography using synchrotron radiation. *IUCrJ*. **2**, 168–176 (2015).

42. T. Weinert *et al.*, Serial millisecond crystallography for routine room-temperature structure determination at synchrotrons. *Nat. Commun.* **8**, 542 (2017).

43. M. Liang *et al.*, The Coherent X-ray Imaging instrument at the Linac Coherent Light Source. *J. Synchrotron Radiat.* **22**, 514–519 (2015).

44. M. P. Minitti *et al.*, Optical laser systems at the Linac Coherent Light Source. *J. Synchrotron Radiat.* **22**, 526–531 (2015).

45. M. R. Bionta *et al.*, Spectral encoding of x-ray/optical relative delay. *Opt. Express*. **19**, 21855–21865 (2011).

46. B. Schmidt *et al.*, Excited-state dynamics of bacteriorhodopsin probed by broadband femtosecond fluorescence spectroscopy. *Biochim. Biophys. Acta BBA - Bioenerg.* **1706**, 165–173 (2005).

47. A. C. Florean *et al.*, Control of retinal isomerization in bacteriorhodopsin in the high-intensity regime. *Proc. Natl. Acad. Sci.* **106**, 10896–10900 (2009).

48. V. I. Prokhorenko *et al.*, Coherent Control of Retinal Isomerization in Bacteriorhodopsin. *Science*. **313**, 1257–1261 (2006).

49. A. Barty *et al.*, Cheetah: software for high-throughput reduction and analysis of serial femtosecond X-ray diffraction data. *J. Appl. Crystallogr.* **47**, 1118–1131 (2014).

50. D. Damiani *et al.*, Linac Coherent Light Source data analysis using psana. *J. Appl. Crystallogr.* **49**, 672–679 (2016).

51. T. A. White *et al.*, CrystFEL: a software suite for snapshot serial crystallography. *J. Appl. Crystallogr.* **45**, 335–341 (2012).

52. W. Brehm, K. Diederichs, Breaking the indexing ambiguity in serial crystallography. *Acta Crystallogr. D Biol. Crystallogr.* **70**, 101–109 (2014).

53. A. J. McCoy *et al.*, Phaser crystallographic software. *J. Appl. Crystallogr.* **40**, 658–674 (2007).

54. P. Emsley, K. Cowtan, *Coot* : model-building tools for molecular graphics. *Acta Crystallogr. D Biol. Crystallogr.* **60**, 2126–2132 (2004).

55. P. D. Adams *et al.*, *PHENIX* : building new software for automated crystallographic structure determination. *Acta Crystallogr. D Biol. Crystallogr.* **58**, 1948–1954 (2002).

56. P. Emsley, B. Lohkamp, W. G. Scott, K. Cowtan, Features and development of Coot. *Acta Crystallogr. D Biol. Crystallogr.* **66**, 486–501 (2010).

57. M. Schmidt, in *Ultrashort Laser Pulses in Biology and Medicine* (Springer, Berlin, Heidelberg, 2008; https://link.springer.com/chapter/10.1007/978-3-540-73566-3_9), *Biological and Medical Physics, Biomedical Engineering*, pp. 201–241.

58. U. K. Genick *et al.*, Structure of a protein photocycle intermediate by millisecond time-resolved crystallography. *Science*. **275**, 1471–1475 (1997).

59. R. A. Mathies, C. H. Brito Cruz, W. T. Pollard, C. V. Shank, Direct observation of the femtosecond excited-state cis-trans isomerization in bacteriorhodopsin. *Science*. **240**, 777–779 (1988).

60. E. F. Pettersen *et al.*, UCSF Chimera--a visualization system for exploratory research and analysis. *J. Comput. Chem.* **25**, 1605–1612 (2004).

61. J. M. Glownia *et al.*, Time-resolved pump-probe experiments at the LCLS. *Opt. Express*. **18**, 17620–17630 (2010).

Figures:

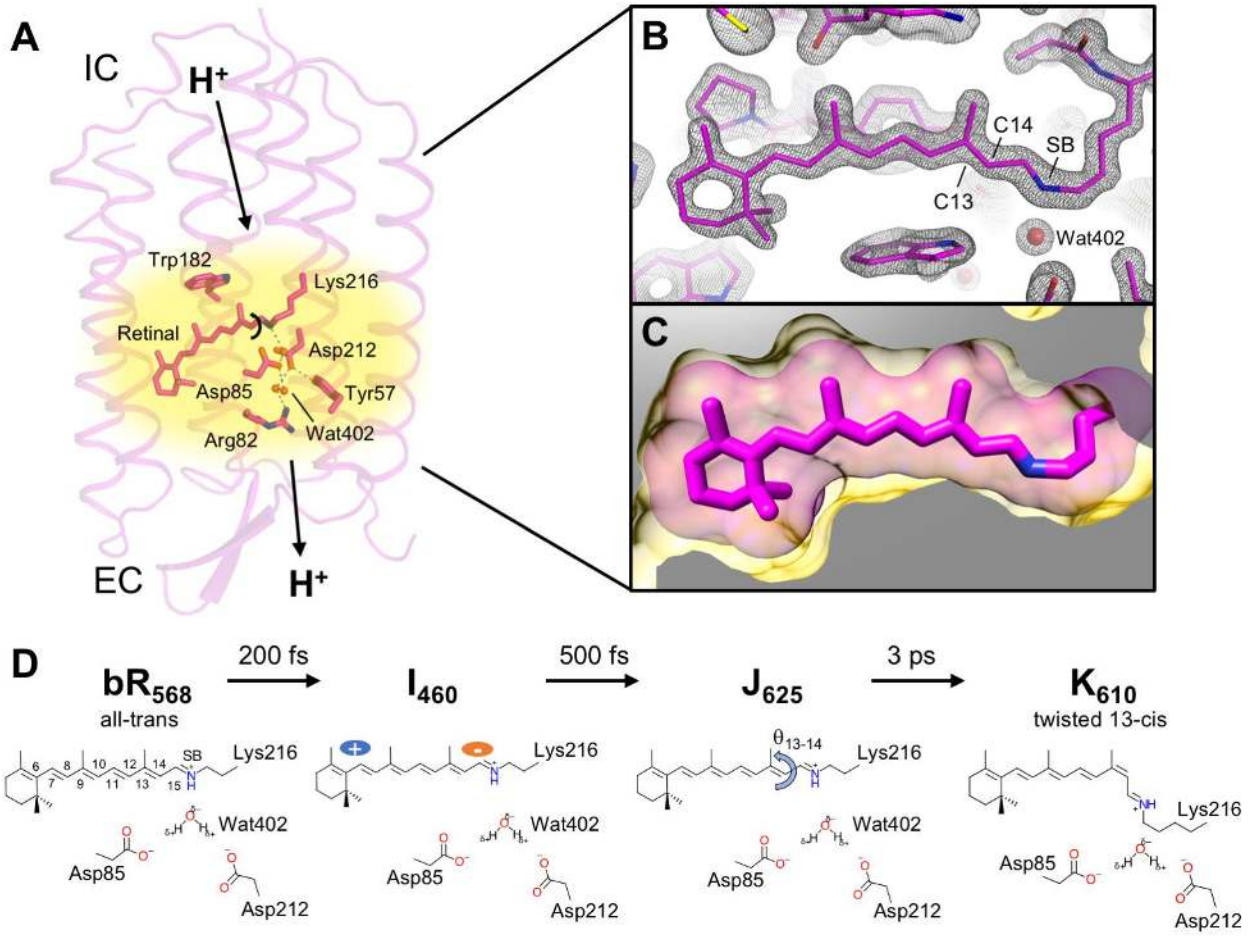

Figure 1: Early events in bR activation. (**A**) Structural changes in the seven transmembrane helix proton-pump bR are initiated by the *trans*-to-*cis* isomerization of the covalently bound retinal chromophore. The arrows indicate direction of H^+ transport from cytoplasmic side (IC) to extracellular side (EC) of the membrane. A hydrogen bonding network including the complex counter-ion network and several water molecules is critical for maintaining the high affinity of the Schiff base (SB) link for protons. (**B**) Serial femtosecond crystallography allows us to resolve the retinal molecule and its binding pocket with near atomic resolution ($2F_{obs}$-F_{calc} electron density of the light-adapted resting state at 1.5 Å resolution shown in blue at 2σ) at ambient temperature and in the membrane-like environment of lipidic cubic phases. The atoms C13 and C14 are labelled to indicate the bond undergoing isomerization. (**C**) The retinal chromophore (sticks with van der Waals radii shown as transparent halo) is tightly encased within the binding pocket of the bR dark state (yellow). (**D**) Retinal isomerization is an ultrafast event progressing within picoseconds from the bR dark state over the I and J to the K intermediate. I forms within about 200 fs after excitation and is characterized by a rapid rise in the retinal dipole moment (*5*) and twisting of the polyene backbone (*6*). After about 500 fs the J intermediate evolves which initiates the isomerization reaction (*7*) and turns into the K state with isomerized 13-*cis* retinal after about 3 ps (*8*). The ultrafast dynamic interplay between retinal and its binding pocket increases quantum efficiency and guides stereo selectivity of retinal isomerization.

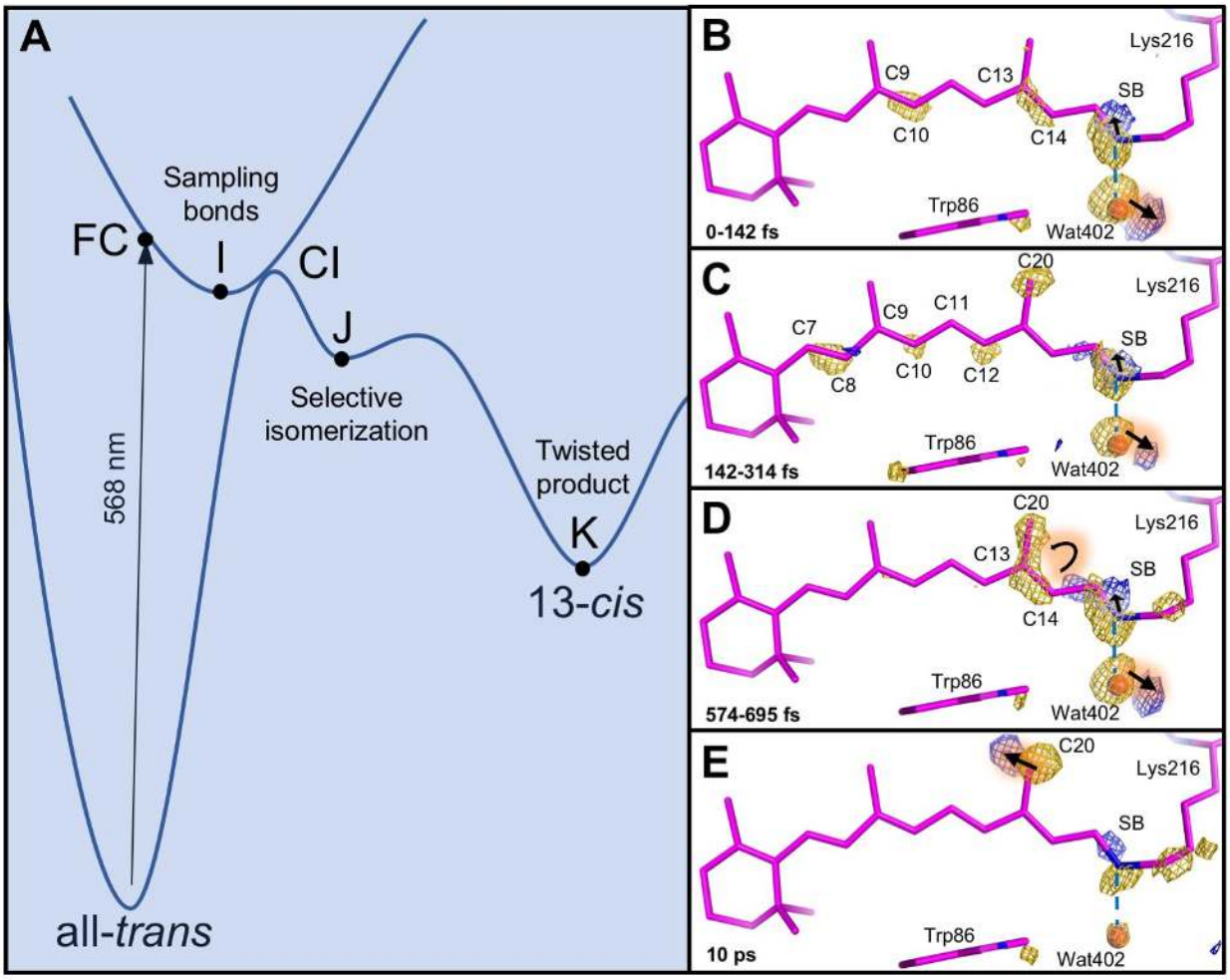

Figure 2: Femtosecond structural dynamics along the retinal chromophore. The potential energy diagram (**A**) indicates along energy (y-axis) and reaction coordinates (x-axis) how absorption of a photon promotes all-*trans* retinal to the Franck Condon point (FC). The excitation energy is kinetically dissipated after passage through the conical intersection (CI). *Trans-cis* isomerization occurs along local energy minima correlating with the I, J and K spectroscopic intermediates. According to the commonly accepted model, the transition of the excited state intermediate (I) to the first ground state product (J) occurs within about 0.5 ps and coincides with the onset of retinal isomerization (*7*, *27*, *59*). The progression (**B-E**) of difference Fourier electron density (F_{obs}^{light} - F_{obs}^{dark} contoured at 4 σ, golden negative, blue positive) displayed along a dark state model allows us to follow *trans-cis* transition and see how the double bond system is sampled immediately after photoactivation before selective isomerization around the C13=C14 bond occurs. The process results into an energetically elevated 13-*cis* isomer that is still twisted by the protein binding pocket 10 ps after activation. All temporal snapshots of this trajectory are available as **Movie S2.**

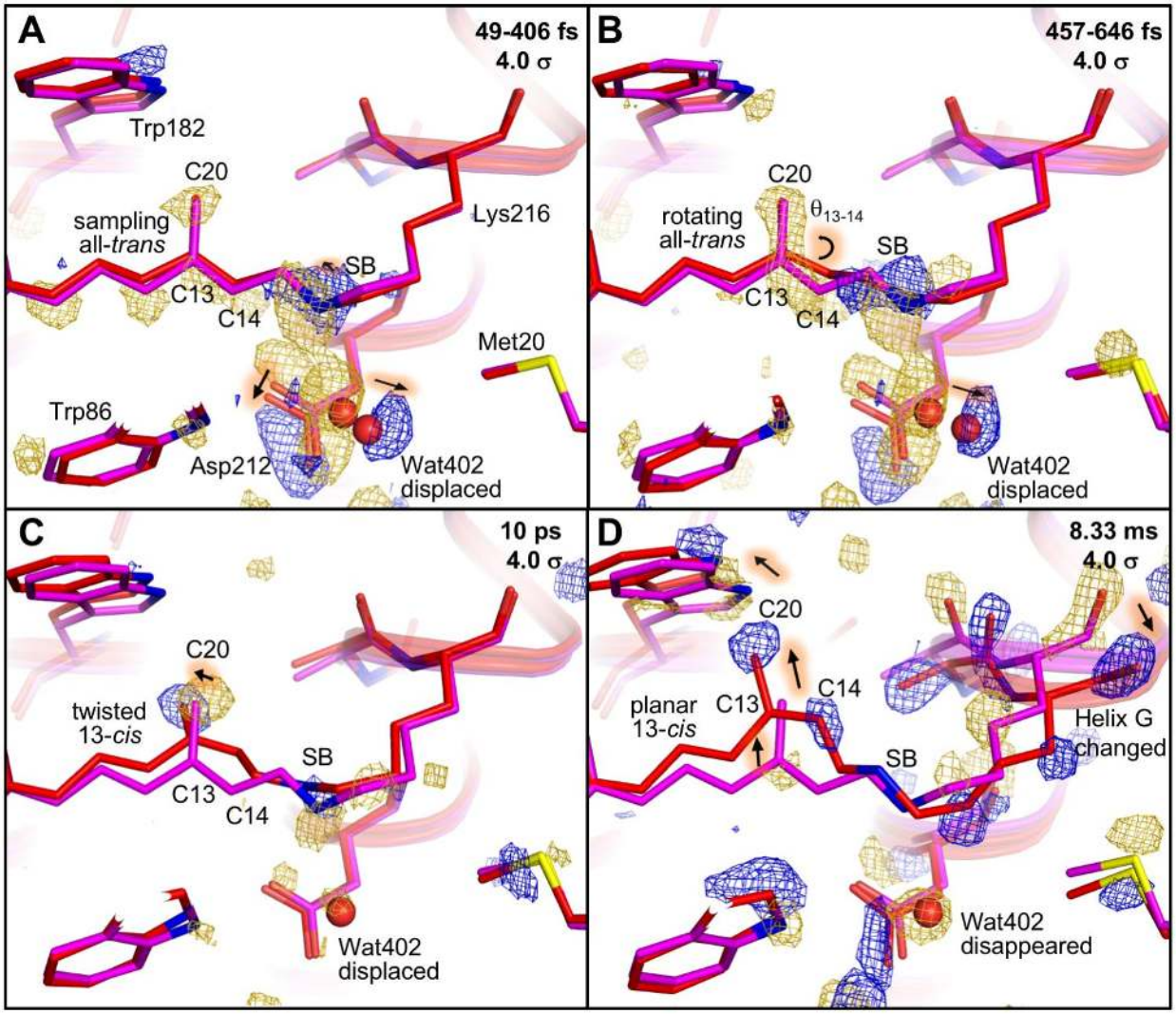

Figure 3: Structural intermediates at pump-probe delays (Δt) corresponding to times where key spectral intermediates of the bR photocycle occur. (**A**) Δt= 49-406 fs ≈ I-intermediate (**B**) Δt= 457-646 fs ≈ J-intermediate (**C**) Δt = 10 ps ≈ K-intermediate and (**D**) Δt = 8.33 ms ≈ M-intermediate. The structure of the bR dark state is shown in magenta and overlaid with the bR reaction intermediates in red. The difference Fourier electron density map (F_{obs}^{light} - F_{obs}^{dark} contoured at 4 σ, golden negative, blue positive) and arrows indicate the structural rearrangements around the isomerizing C13=C14 bond and the retinal counter-ion. The corresponding extrapolated electron density maps $2F_{ext}$-F_{calc} are available as **Figure S3 and Movie 1.**

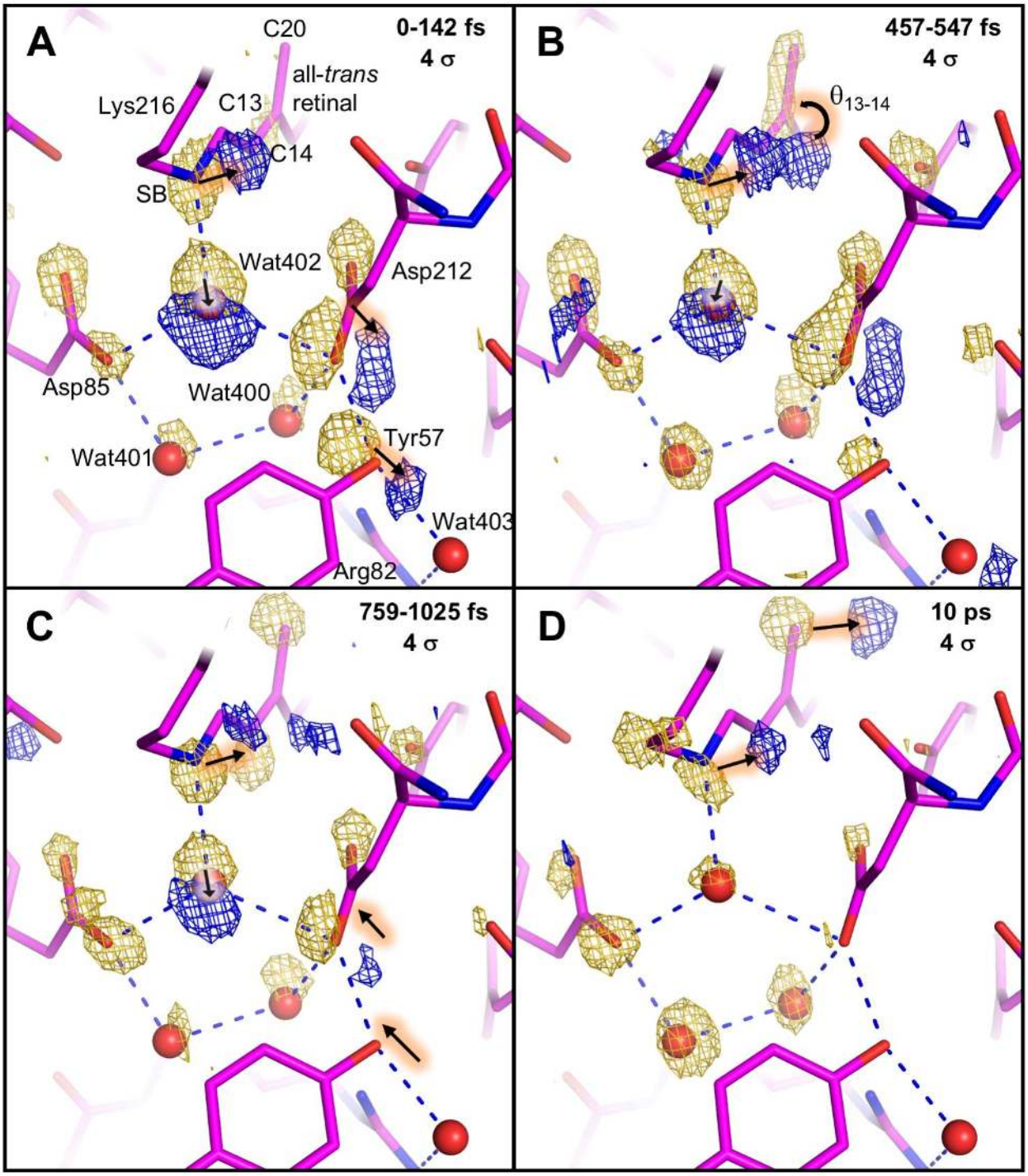

Figure 4: Close-up view of the protonated Schiff base (SB) and associated counter-ion network. Progression of the difference Fourier electron density map (F_{obs}^{light} - F_{obs}^{dark} contoured at 4 σ, golden negative, blue positive) shows the coherent motions of the hydrogen bonding network connecting the Schiff base with Asp85, Asp212, Tyr57 via water molecules Wat402, Wat401 and Wat400. Arrows indicated correlated motions in retinal and hydrogen bonding network. The sticks represent the dark state model of bR. All temporal snapshots are available as **Movie S3.**

Movie Captions:

Movie 1: Retinal isomerization in refined structures with extrapolated electron density ($2F_{ext}$ - F_{calc} contoured at 1.2 σ).

Movie 2: Dynamic view of retinal isomerization and response of the counter-ion network. The movie shows the transitions between four structural intermediates: Ground State, Δt = 49 - 406 fs, Δt = 457 - 646 fs and Δt = 10 ps. The morphs between the refined structures where generated with Chimera (*60*) and reveal a fast motion proceeding through the entire structure followed by a slower rearrangement. A zoom into the region of the counter-ion network highlights the hydrogen bond breakage between the Schiff base and Wat402. The detailed view of the retinal isomerization visualizes the structural rearrangements as the isomerization proceeds. Time scales in the movie do not correlate to real time scales and the structures are linear morphs of atom motions. The transition 457 - 646 fs → 10 ps is shown slower than the other two transitions in order to highlight the longer time scale of the transition.

Science
AAAS

Supplementary Materials for

Retinal isomerization in bacteriorhodopsin captured by a femtosecond X-ray laser

Przemyslaw Nogly, Tobias Weinert, Daniel James, Sergio Carbajo, Dmitry Ozerov, Antonia Furrer, Dardan Gashi, Veniamin Borin, Petr Skopintsev, Kathrin Jaeger, Karol Nass, Petra Båth, Robert Bosman, Jason Koglin, Matthew Seaberg, Thomas Lane, Demet Kekilli, Steffen Brünle, Tomoyuki Tanaka, Wenting Wu, Christopher Milne, Thomas White, Anton Barty, Uwe Weierstall, Valerie Panneels, Eriko Nango, So Iwata, Mark Hunter, Igor Schapiro, Gebhard Schertler, Richard Neutze, Jörg Standfuss*

*Correspondence to: joerg.standfuss@psi.ch

This PDF file includes:

Figs. S1 to S8
Tables S1 to S3
Captions for Movies S1 to S3

Other Supplementary Materials for this manuscript include the following:

Movies S1 to S3

Supplementary Figures:

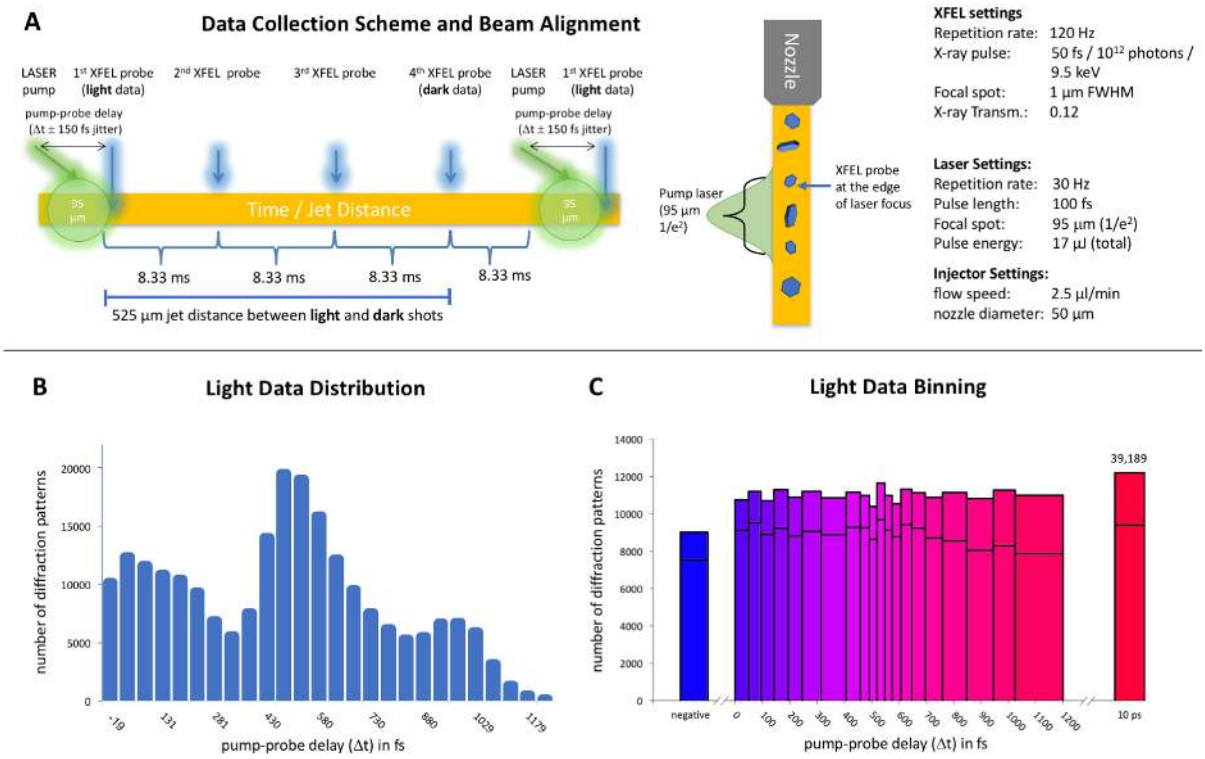

Figure S1: Collection and sorting of diffraction data. (**A**) The schematic on the left shows the pump-probe scheme employed for time-resolved data collection. Blue arrows indicate the XFEL probe pulses that occur every 8.33 ms at the LCLS frequency of 120 Hz. The green arrows indicate the pump laser pulses, that occur before every fourth XFEL probe pulse with a set pump-probe delay (Δt). The pump laser (green circle) was operated at 30 Hz to allow enough time to clear away activated sample. The schematic on the right shows the X-ray alignment with respect to the pump laser. The X-ray interaction region is offset by 50 µm with respect to the center of the pump laser to further ensure that completely unpumped crystals are probed for the collection of dark data. As a side effect crystals are pumped using the less intense tail of the pump laser. (**B**) The exact value of Δt is subject to a jitter of ± 150 fs, leading to a Gaussian distribution around the nominal delay times. By collecting data at different Δt values (-500 fs, 300 fs, 600 fs, 900 fs, 1100 fs and 10 ps) and sorting the images using the LCLS timing-tool the complete sub-picosecond range can be covered. (**C**) Sorting of the data into bins with the same number of diffraction patterns allows to calculate structural snapshots of comparable quality. The chosen bins are shown with a colour gradient from blue for negative timing data to red for data collected at 10 ps. The negative bin (blue bar on the left) contains all data recorded at a target time of -500 fs and are used as a negative control. The 10 ps data (red bar on the right) are depicted in a different scale. The number of collected patterns is indicated above the bar. The horizontal line in each bar indicates the number of patterns that were indexed for each bin (typically about 80% of collected hits). Structural snapshots in the first picosecond are calculated from 3 bins each to maintain a comparable number of images as used for the 10 ps time point (~30'000 diffraction patterns). For the structural refinement at delay times corresponding to the I and J intermediates **(Figure 3)**, we combined data from 6 bins resulting into about 60'000 diffraction patterns for each intermediate.

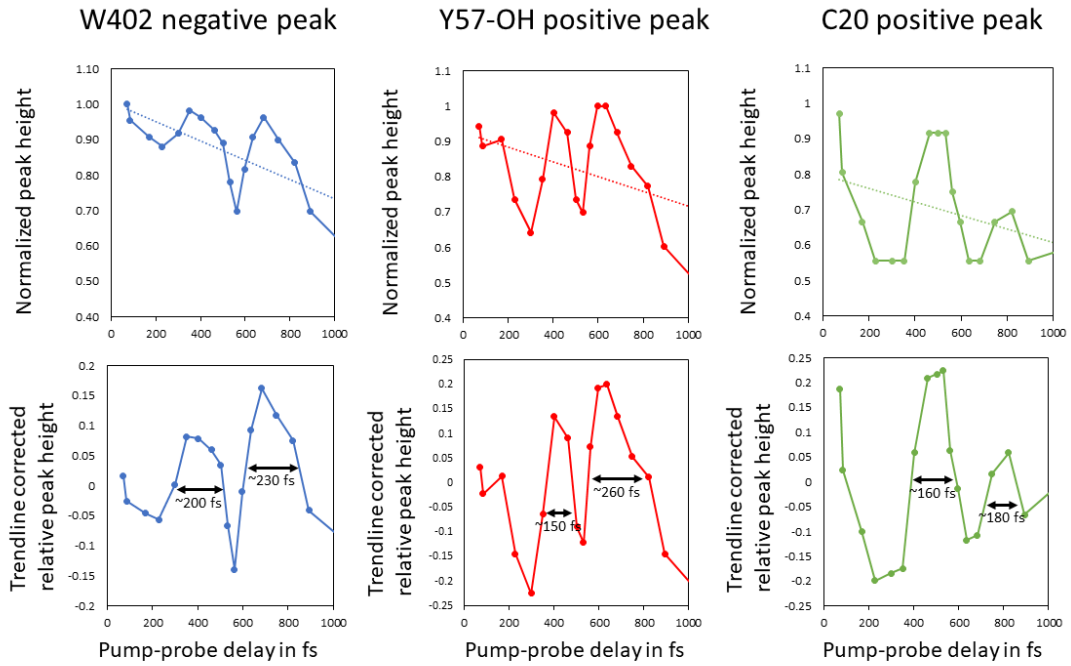

Figure S2: Estimation of time resolution based on difference density peaks associated with the counter-ion hydrogen bonding network. Timing of two different laser sources such as an XFEL and the TI:Sapphire pump laser is subject to a temporal jitter. The current LCLS setup which monitors the arrival of electron bunches and couples this information to the pump laser partially alleviates that problem, resulting in timing jitter with a root mean square deviation between 120 fs (*61*) and 180 fs (*25*, *45*). The temporal resolution of features prior to additional correction has been estimated to be 174 fs (*45*). Additional measurements of the arrival time by spectral encoding allow assigning timestamps to the distributed data, further reducing the root mean square deviation of the timing to around 25 fs (*45*). In our experiment, the pulse duration of 100 fs of the optical laser marks the lower end of the achievable timing resolution.

The true timing resolution is however difficult to estimate and is further blurred by the complexity of a biological system, which makes it safe to assume that time resolution is not limited by the jitter which we corrected for by using the spectral encoding timing tool implemented at CXI. Another way to estimate time resolution is to analyze variations in difference density peaks in the hydrogen bonding network of water 402. Related intensities given in **Supporting Data File 1** have been normalized to the strongest peak and plotted against time. (**upper panels**) Features generally decay within the first picosecond (horizontal dotted line), yet the decay is associated with a vibrational fluctuation with a period of about 200 fs. (**lower panels**) These peak fluctuations vary in their full width half maximum, but center at around 200 fs, suggesting that features developing on this time scale can be clearly resolved. These observations were confirmed by comparing randomly split half datasets.

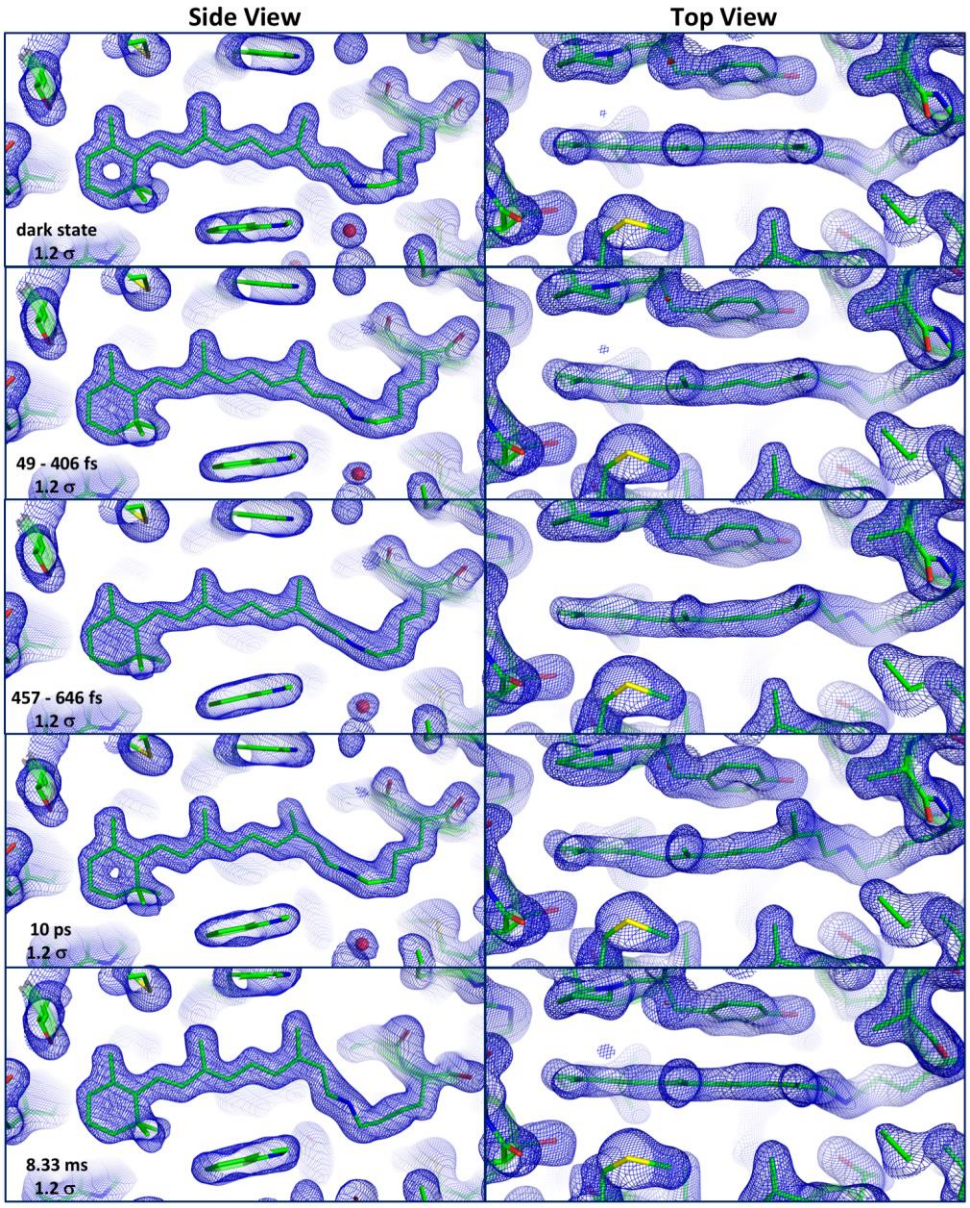

Figure S3: Extrapolated electron density maps ($2F_{ext}$ - F_{calc}) at 1.2 σ level and refined structures at time delays corresponding approximately to the I, J, K and M intermediates in comparison to the dark state ($2F_{obs}$ - F_{calc}).

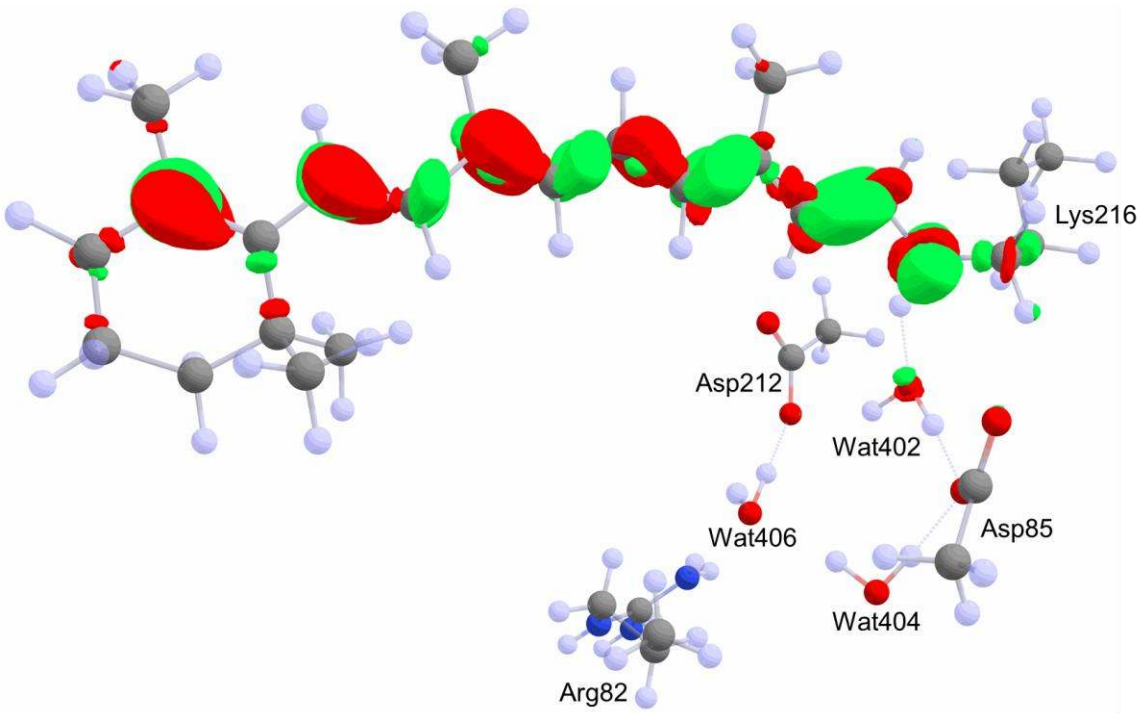

Figure S4: Changes in electron density upon excitation. The S1-S0 electron density difference at the dark state geometry (Frank-Condon point) is visualized in order to evaluate the effect of the photon absorption. The quantum chemical subsystem comprised the retinal chromophore, Lys216, Asp85, Asp212, Wat402, Arg82, Wat404, Wat406 and was described at the CAM-B3LYP/cc-pVTZ level of theory. We observe that upon excitation to S1, the π-electron density is moving from the left side (β-ionone ring, green color corresponds to the negative change in electron density) to the right side (Schiff base region, red color correspond to the positive change in electron density), while the sigma density is moving in the opposite direction. In addition, we also note a portion of electron density extending to Wat402 that is hydrogen bonded to the Schiff base. The change in the retinal dipole moment thus perturbs the hydrogen bond which leads to a repulsion, the repulsion is then further enhanced during the dynamics part of the simulation explaining why Wat402 is displaced as immediate response to the photo excitation.

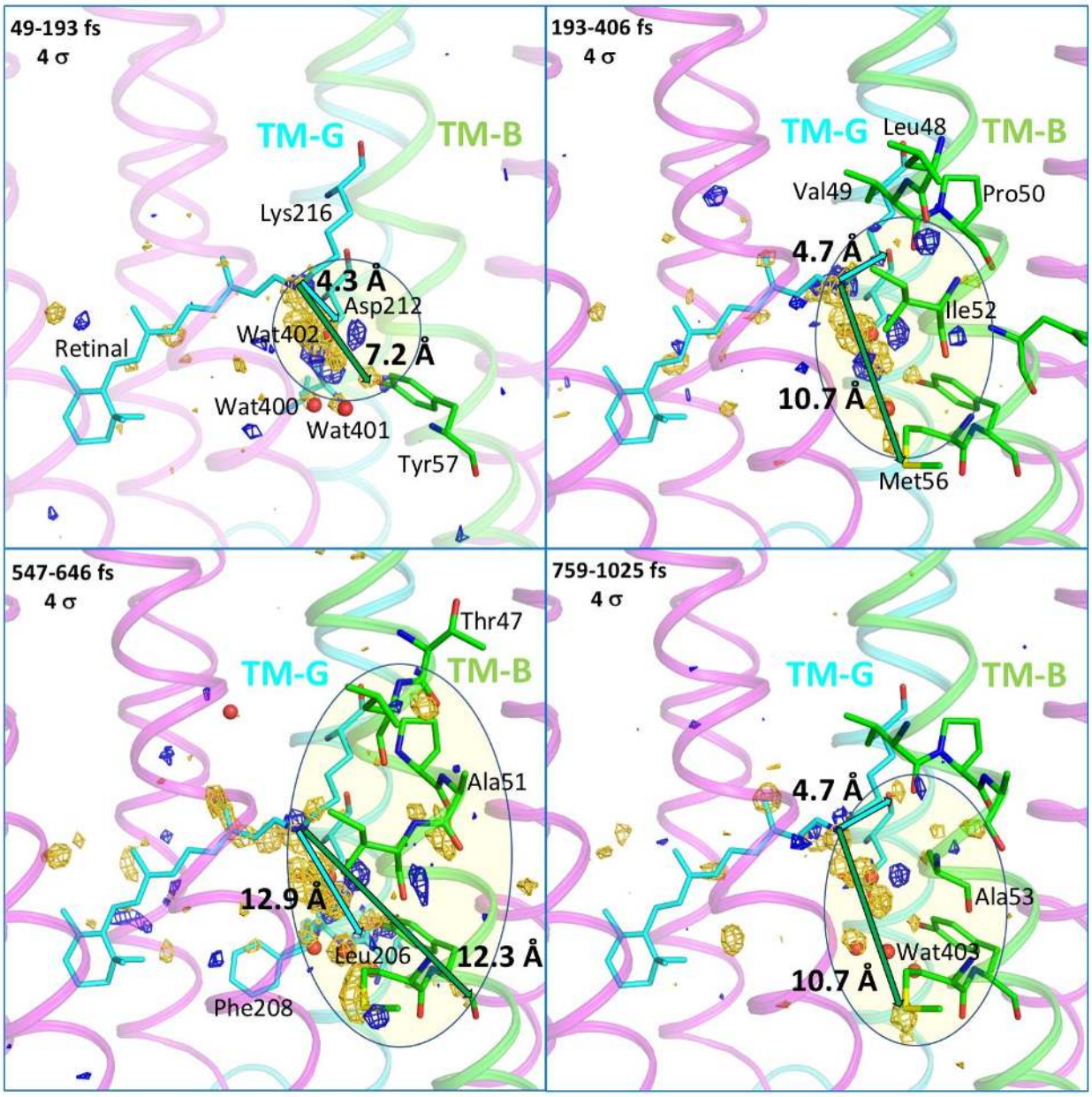

Figure S5: Evolution of difference density features (F_{obs}^{light} - F_{obs}^{dark} contoured at 4 σ, golden negative, blue positive) along transmembrane helices G (cyan) and B (green). Residues of helices B and G with strong densities above 4 σ are shown as sticks. The strong density peaks along helices G and B are highlighted with an oval and arrows indicate the furthest distance of the strong difference density features along the two helices.

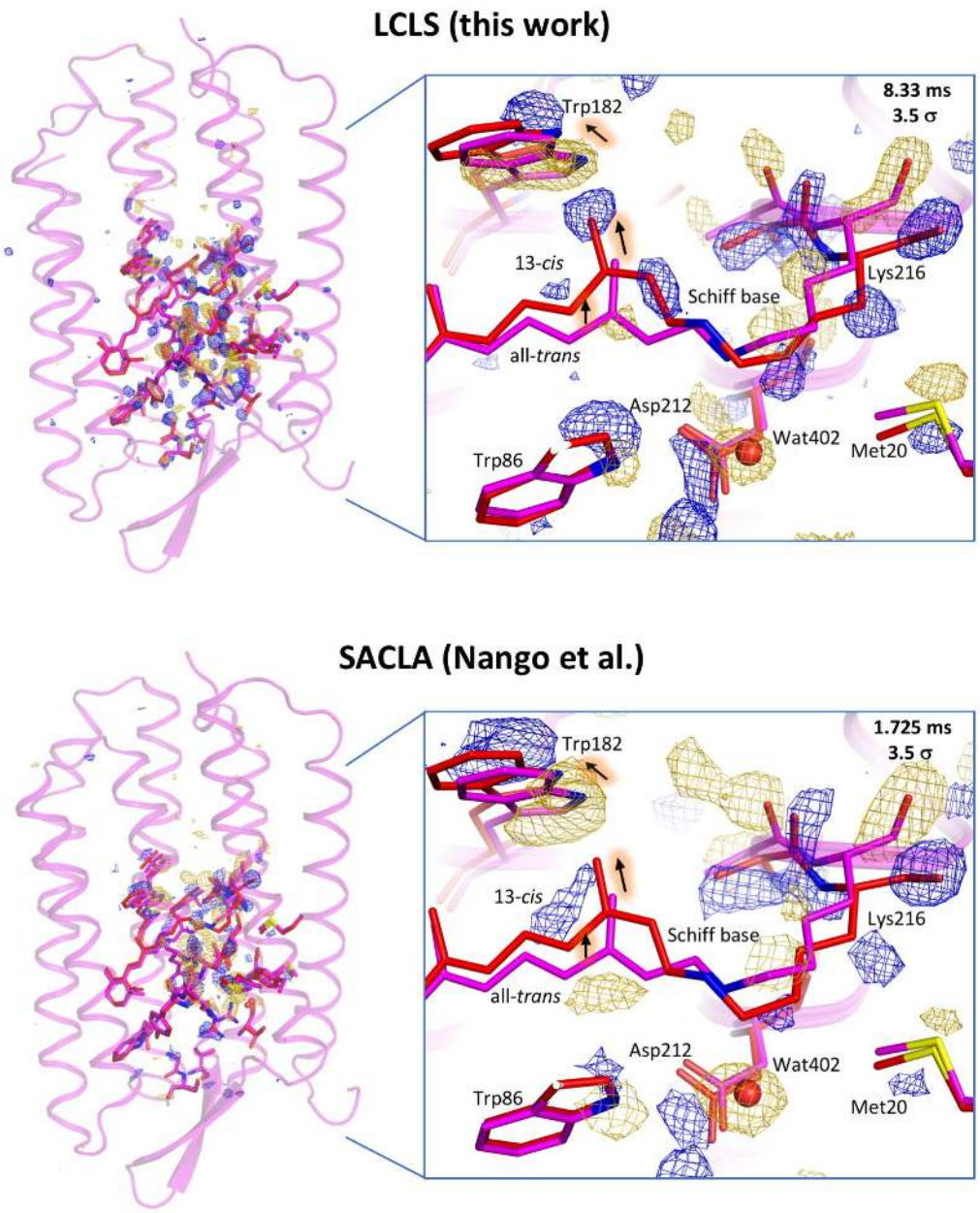

Figure S6: Comparison of bR structures in the millisecond range obtained at LCLS and SACLA (*19*). Both the difference Fourier maps (F_{obs}^{light} - F_{obs}^{dark} contoured at 3.5 σ, golden negative, blue positive) obtained 8.33 ms after activation at LCLS (upper left) and the 1.725 ms map obtained at SACLA (lower left) indicate comparable conformational changes around the retinal binding pocket. Refinement (enlargements) of the dark (magenta) and photo activated states (red) results into near identical structures (Cα root mean square deviation = 0.31 $Å^2$) with planar 13-*cis* retinal. The 8.33 ms structure was refined against the extrapolated structure factors, while the 1.725 ms was refined against the observed data with an alternative conformation approach for light and dark state contributions.

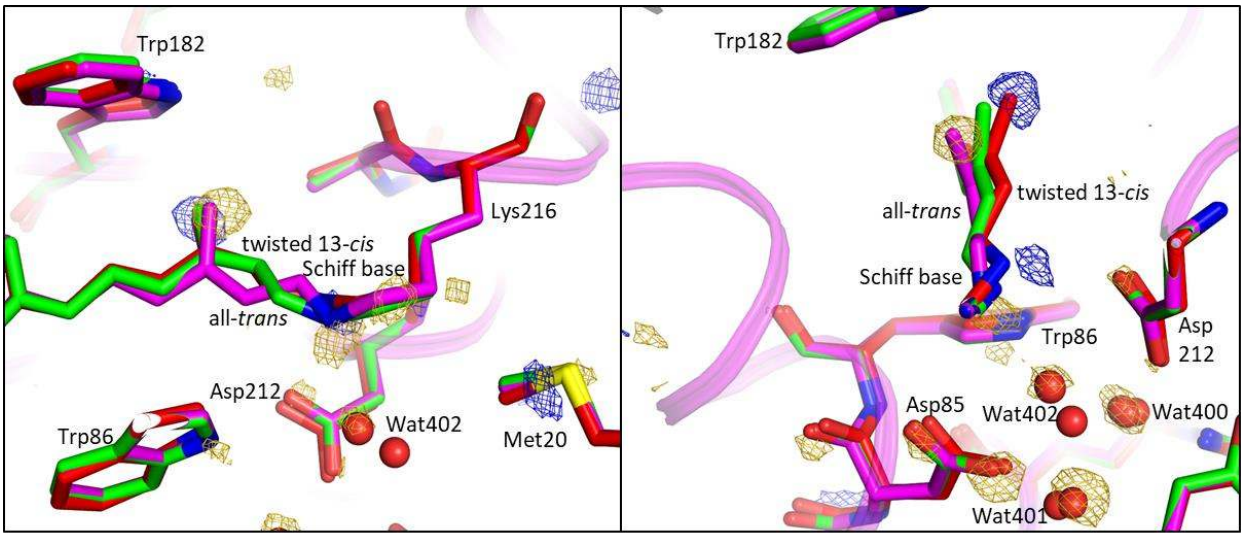

Figure S7: Comparison of bR structures obtained with femtosecond laser at LCLS and nanosecond laser at SACLA. The panels show two views of the bR dark state (magenta) and the structural intermediates obtained after refining data with 16 ns time delay collected at SACLA (green, (*19*)) and 10 ps collected at LCLS (red, this work). The structures are overlaid with the difference Fourier map ($F_{obs}^{light} - F_{obs}^{dark}$ contoured at 4.0 σ, golden negative, blue positive) obtained at LCLS.

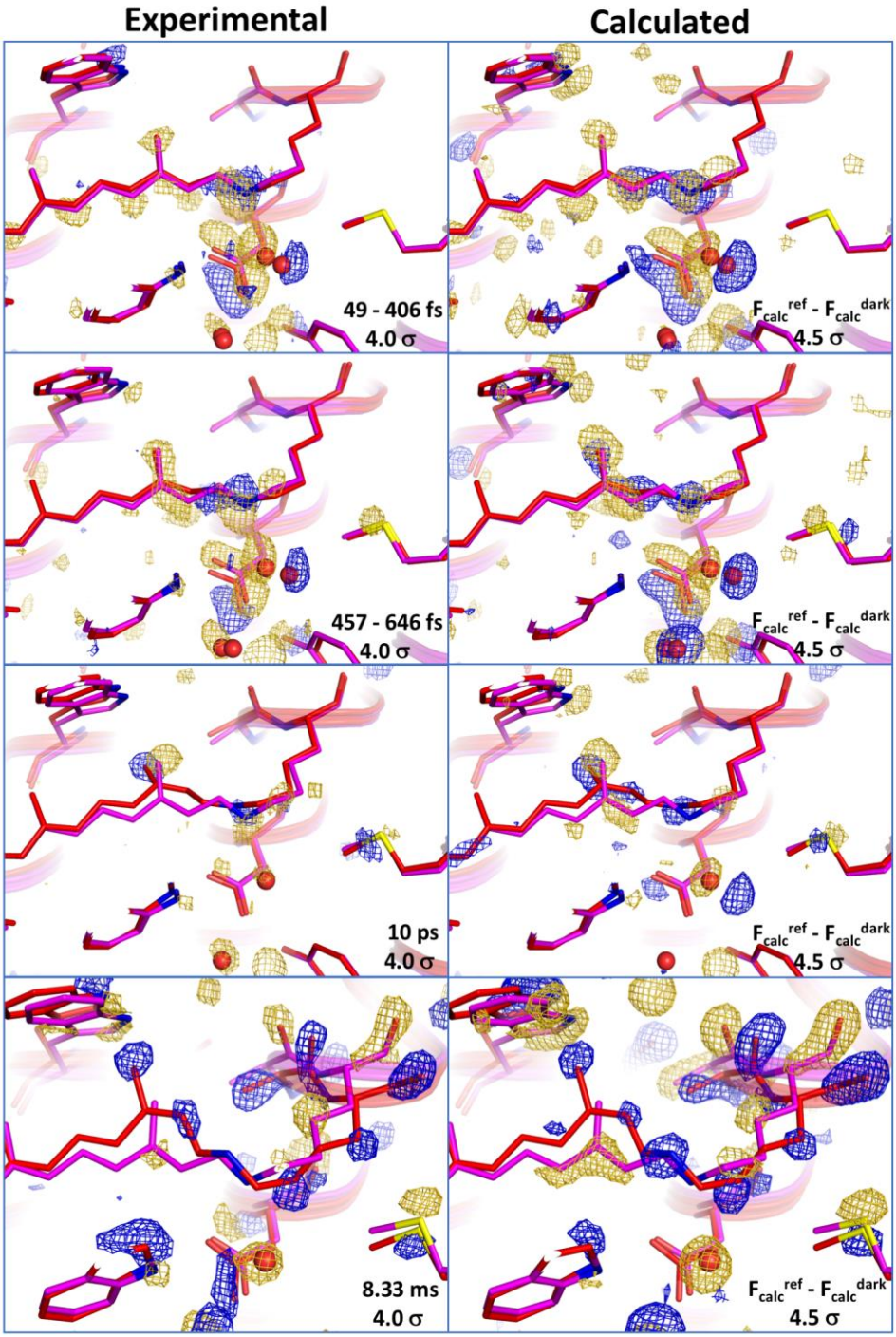

Figure S8: Comparison of experimental (**left**) and calculated (**right**) difference densities. Both the maps based on experimental data (F_{obs}^{light} - F_{obs}^{dark}) and the ones calculated from the structure factor ($F_{calc}^{refined}$ - F_{calc}^{dark}) differences between dark state and refined intermediates show overall the same density features providing a control for the structural refinement based on extrapolated structure factors.

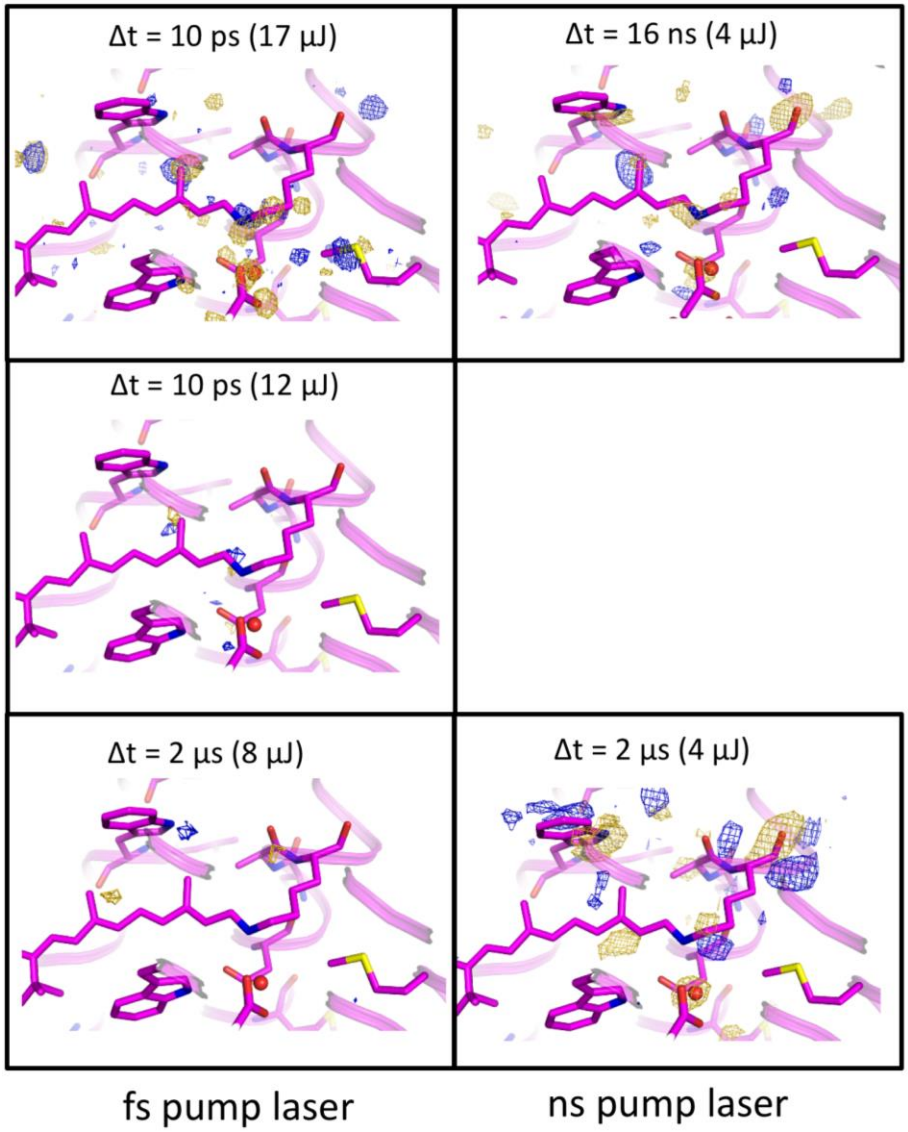

Figure S9: Consideration of laser energy used in previous TR-SFX experiments. Since our initial experiment to demonstrate the viability of lipidic cubic phase injectors for time-resolved crystallography (*41*) we have performed a series of pump-probe experiments at X-ray lasers to elucidate the activation of bacteriorhodopsin including experiments using a nanosecond laser (*19*) and the experiments relying on a femtosecond laser we described in this manuscript. Results are difficult to compare directly because of variations in the experimental setup, sample preparation and data quality between different beamtimes. However, difference Fourier maps (F_{obs}^{light} - F_{obs}^{dark} contoured at 3.5 σ, golden negative, blue positive, selected side chains shown as sticks) resulting from previous beamtimes using the LCLS femtosecond laser (left side) suggested that laser energy below a certain threshold does not result into interpretable difference peaks. Two difference Fourier maps calculated from data collected using the nanosecond laser pump-probe setup at SACLA are shown as a reference. As a side note, in the experiment with the ns laser we illuminated the jet from two sides which made it more efficient, while a similar setup was not possible in the limited space of the LCLS vacuum chamber.

Table S1: Table crystallographic data.

Dataset (Δt range)	Dark	Negative	0-141 fs	49-193 fs	94-245 fs	141-314 f	193-406 fs	245-458 fs	314-490 fs	406-518 fs	457-547 fs	490-574 fs	518-606 fs	547-646 fs	574-695 fs	606-759 fs	646-847 fs	695-946 fs	759-1025 fs	847-1201 fs	10ps	8.3 ms
Space group	P63																					
Unit cell (a=b; c; α=β; γ)	62.32; 111.1; 90; 120																					
Hits	298781	9024	32657	33205	32900	33389	32946	33203	32987	32524	33017	33018	33176	32840	32994	33329	33160	32847	33242	33096	39189	304392
Indexed patterns	241475	7540	27584	27684	26971	27136	26795	27256	27448	27205	27615	27475	27608	27340	27462	27402	26535	25350	24928	24240	30245	235238
Indexing rate (%)	80.8	83.4	84.5	83.5	81.9	81.3	81.2	82.1	83.2	83.6	83.5	83.2	83.2	83.3	83.4	82.4	80.2	77.2	75.0	73.3	77.2	77.3
Overall statistics (resolution range in Å)	19.35 – 1.50																					**19.35 – 1.55**
Total number of reflections	78345217	2773962	9628607	9723983	9386027	9233235	8809665	8604018	8420641	8253090	8434496	8459497	8544881	8568043	8648571	8753753	8475542	8134355	7991072	7719144	8881180	72507747
Number of unique reflections	39064	38836	39062	39063	39063	39062	39061	39064	39062	39063	39060	39061	39060	39054	39050	39048	39039	39030	39024	39034	39037	35438
Completeness (%)	100.00	99.41	100.00	100.00	100.00	100.00	100.00	100.00	100.00	100.00	100.00	100.00	100.00	99.97	99.96	99.96	99.94	99.91	99.89	99.92	99.93	100.00
Multiplicity	2005.6	75.05	247.0	249.3	240.7	236.9	226.1	220.9	216.2	212.1	216.8	217.5	220.1	221.0	223.5	226.6	220.4	212.1	208.4	201.4	230.5	2046.2
Rsplit	2.7	14.4	7.3	7.3	7.5	7.3	7.6	7.7	7.8	8.1	7.9	7.93	7.9	7.8	7.7	7.6	7.6	7.8	8.0	8.4	7.6	2.8
CC 1/2	0.999	0.978	0.994	0.994	0.994	0.995	0.993	0.990	0.993	0.988	0.991	0.993	0.993	0.994	0.994	0.993	0.994	0.990	0.992	0.991	0.993	0.999
*CC**	0.999	0.995	0.998	0.998	0.998	0.999	0.998	0.997	0.998	0.997	0.998	0.998	0.998	0.998	0.998	0.998	0.998	0.997	0.998	0.998	0.998	0.999
<I/σ(I)>	19.0	3.9	6.9	6.9	6.8	6.7	6.6	6.5	6.4	6.4	6.4	6.4	6.4	0.63	6.3	6.1	6.1	6.0	5.9	5.8	6.4	19.6
High resolution statistics (resolution range in Å)	1.55 – 1.50																					**1.62 – 1.55**
Number of unique reflections	3893	3680	3891	3892	3893	3892	3891	3893	3892	3892	3889	3890	3889	3883	3879	3878	3868	3860	3854	3864	3867	3535
Completeness (%)	100.00	94.53	99.95	99.97	100.00	99.97	99.95	100.00	99.97	99.97	99.90	99.92	99.90	99.74	99.64	99.61	99.36	99.15	99.0	99.26	99.33	100.00
Multiplicity	122.6	5.9	17.3	17.8	17.3	16.4	15.4	14.7	14.4	13.9	13.7	13.5	13.2	12.2	11.2	10.6	9.7	9.1	8.8	8.9	10.0	216.2
Rsplit	63.8	179.7	122.9	125.2	123.3	129.0	128.8	137.6	145.0	140.9	150.7	155.9	161.4	168.7	160.9	171.5	184.5	185.6	177.9	187.6	195.7	143.5
CC 1/2	0.084	0.150	0.292	0.290	0.267	0.238	0.331	0.276	0.231	0.244	0.220	0.225	0.221	0.207	0.232	0.151	0.040	0.044	0.086	0.188	0.166	0.047
*CC**	0.394	0.51	0.672	0.670	0.649	0.620	0.705	0.658	0.613	0.626	0.601	0.607	0.602	0.585	0.614	0.512	0.278	0.292	0.397	0.562	0.534	0.301
<I/σ(I)>	2.3	n.d.	1.0	1.0	1.0	0.9	0.9	0.8	0.8	0.8	0.8	0.8	0.8	0.7	0.7	n.d.	0.8	0.8	0.8	0.7	0.5	3.1

Random half data sets for CC and R_{split} calculations are obtained by merging every reflection hkl from all odd numbered indexed diffraction patterns of a given dataset into one dataset and all even numbered patterns into another by using the monte carlo integration.

$$R_{split} = \frac{1}{\sqrt[2]{2}} \frac{\sum |I_{even} - I_{odd}|}{\frac{1}{2}\sum (I_{even} + I_{odd})}$$

Dataset Δt range	Dark	49 - 406 fs	457 - 646 fs	10 ps	8.33 ms
Space group			$P6_3$		
Unit cell **(a=b in Å; c in Å; α=β in °; γ in °)**			62.32; 111.10; 90; 120		
Wavelength (Å)			1.3		
Data resolution overall **(Data resolution highest shell)** **in Å**			19.35 – 1.50 (1.55 – 1.50)		19.35 – 1.55 (1.62 – 1.55)
Number of indexed patterns	241475	54479	54955	30245	235238
Rsplit	2.71 (63.8)	5.30 (89.46)	5.54 (109.59)	7.56 (195.7)	2.76 (143.5)
I/σI	18.97 (2.26)	9.47 (1.25)	8.95 (1.04)	6.36 (0.54)	19.62 (3.1)
CC 1/2	0.999 (0.084)	0.997 (0.503)	0.996 (0.123)	0.993 (0.166)	0.999 (0.047)
CC*	0.999 (0.394)	0.999 (0.818)	0.999 (0.734)	0.998 (0.534)	0.999 (0.301)
Multiplicity	2005.6 (122.6)	474.4 (33.1)	435.2 (25.9)	230.5 (10.0)	2046.2 (216.2)
Completeness	100 (100)	100 (100)	100 (100)	100 (99.33)	100 (100)
Activation level (%)	0	25	18	16	10
Refinement resolution[#]	19.35 – 1.50	18.5 – 1.90	18.5 – 1.90	18.1 – 1.90	18.5 – 1.90
No. reflections used in refinement	38964	18848	18326	18261	18134
R_{work} / R_{free}	0.115 / 0.143	0.173 / 0.231	0.205 / 0.264	0.250 / 0.299	0.224 / 0.272
Ramachandran favored (%)	98.68	98.68	97.81	97.81	100
Ramachandran outliers (%)	0	0.44	0.44	0.44	0
R.m.s.d. Bond length (Å)	0.017	0.012	0.012	0.004	0.004
R.m.s.d. Bond angles (°)	1.403	1.096	1.180	0.619	0.689
PDB entry	6G7H	6G7I	6G7J	6G7K	6G7L

Table S2: Refinement statistics of the dark state and the 49 – 409 fs, 457 – 646 fs, 10ps and 8.33 ms intermediates. [#]Data extrapolation limits the resolution up to which the refinement can be carried out because F_{obs}^{light} - F_{obs}^{dark} difference amplitudes of weaker reflections become unreliable due to low signal-to-noise levels.

Dataset (Δt range)	0-141	49-193	94-245	141-314	193-406	245-458	314-490	406-518	457-547	490-574	518-606	547-646	574-695	606-759	646-847	695-946	759-1025	847-1201	10ps
Retinal + Lys 216																			
C7-C8(-)	-3.4	-3.7	-4.4	-6.4	-6	-5.8	-4.4	-4.2	-3.9	-3.8	-2.9	-3.4	-3.6	-4.1	-4.7	-4.3	-3.8	-3.9	-3.7
C7-C8(+)	3	3.1	2.8	2.8	2.6	2.5	2.8	2	2.5	2	2	2	3	2.5	3.2	3.8	4	3.8	3.9
C9-C10 (-)	-5.4	-5.8	-4.6	-4.5	-4.2	-4.3	-3.8	-3.5	-4	-4	-3.5	-3.8	-4.4	-5.1	-4.9	-5.1	-5.3	-5.4	-3.9
C9-C10 (+)	3	2.8	2.9	4.1	4.5	3.6	3.4	3.2	3.6	2.7	2.6	2.5	2	2.8	3.2	3.5	3	2	2.7
C11-C12 (-)	-3.5	-4.1	-4.8	-5.7	-6.1	-5.9	-5.4	-4.4	-4.7	-3.8	-3.8	-3.3	-4	-5.5	-5.4	-5.1	-3.9	-4.2	-3.5
C11-C12 (+)	3.6	4.8	4.4	3.3	3	2.8	2	2	2.7	3	3.1	3	3	2.6	3	4.2	3.3	3.7	2
C13-C14 (-)	-5	-4.7	-3.9	-3.5	-3.3	-5.3	-5.2	-5.6	-5.7	-6.1	-5.7	-6.2	-6	-5.3	-5.1	-5.1	-5.9	-5.3	-3.9
C13-C14 (+)	2	2.6	3.3	3	3	2.5	3.2	2.9	2.8	3	3	2	2	2.5	2	2.6	2.9	2	2.1
C20 (-)	-4	-4.2	-5.7	-5.7	-4.9	-5.3	-5.1	-5.1	-5.6	-5.2	-5.3	-5.5	-6	-6.1	-5.8	-6.8	-6.4	-5.9	-7.4
C20 Above (+)	3.5	2.9	2.4	2	2	2	2.8	3.3	3.3	3.3	2.7	2.4	2	2	2.4	2.5	2	2.1	3.6
C20 Below (+)	3.7	2.8	3.2	2.8	3.2	3.2	3.7	3.9	3.6	3.7	3.2	3.8	3.7	3.4	2.9	4	4.1	3.9	6
C15-Nζ(-)	-7.2	-7.2	-6.4	-6.5	-7.6	-8.4	-8.3	-8	-7.5	-7.5	-7.3	-7.5	-7.2	-6.1	-6.7	-7.3	-8.1	-7.1	-5.8
C15-Nζ Above(+)	2	2	2	2	2.5	4	4.4	3.6	4.5	4.9	4.9	4.3	3.6	3.6	3.5	4	3.5	3.3	2
C15-Nζ Below (+)	6	4.6	4.8	5.6	6.2	6.3	6.1	5.8	6.3	6.2	5.7	5.8	6.1	5.9	6.1	5.1	5.1	4	5.4
Cε (-)	-2.5	-3	-4.1	-3.6	-3.9	-3.4	-3.5	-4.4	-4.6	-5.2	-4.8	-5.4	-5.3	-4.7	-3.5	-2.5	-3.7	-3.2	-6.1
Cε (+)	2.1	2.4	2.8	2.5	2.2	2.2	2.5	2.9	2.6	2	2.1	2	2.6	2.6	2	2.6	2.6	2	2
Counterion Network																			
Asp 85-Oδ1(-)	-7.4	-8.5	-7.9	-6.9	-6.8	-8.3	-8.6	-8.1	-7	-7.9	-7.8	-7.3	-5.9	-5.8	-6.5	-6.2	-5.9	-5.5	-5.1
Asp 85-Oδ1 (+)	3.3	4.7	4.9	3.5	5.6	4.8	5.6	4.9	3.9	4.7	4.1	4.9	5.5	5.3	4.2	2.8	2.5	2.9	3.4
Asp 85-Oδ2(-)	-5.4	-5.4	-5.8	-5.9	-6	-5.2	-5.8	-5.9	-5.9	-6.2	-5.9	-6	-6	-6.3	-5.8	-6.4	-6.6	-6.9	-6.4
Asp 85-Oδ2(+)	4	4	3.8	3.8	3.7	3.9	4.5	3.8	4.9	3.6	3.6	3.7	3.2	3.6	3.4	2.5	3	2.8	3.1
Asp 85-O(-)	-4.6	-3.4	-2.9	-3	-3.4	-2.9	-3.1	-3.4	-4	-3.1	-3	-3.1	-3.9	-3.9	-3	-2.9	-3.1	-3	-5.2
Asp 85-O(+)	3.3	0	0	0	4.1	2.7	2.8	2.5	0	3.2	3.1	3.3	3.2	3.2	3.5	3.1	0	0	3
Asp 212-Oδ1 (-)	-6.9	-7.8	-7.7	-7.7	-6.2	-5.3	-5.4	-5.8	-5.7	-6.8	-6.2	-6	-5.5	-5.4	-5.7	-5.9	-6.2	-5.6	-4.4
Asp 212-Oδ1 (+)	3.3	3.9	4	4.6	4	4.2	3.6	3.6	4.4	3.8	3.9	3.7	3.9	4.2	3.8	3.5	3.9	4.4	0
Asp 212-Oδ2 (-)	-8.8	-8.4	-7.5	-7.5	-8.3	-9.7	-9.5	-8.9	-9.5	-9.1	-9	-8.2	-8.8	-9.1	-9.2	-8.5	-6.5	-5.1	-4.3
Asp 212-Oδ2 (+)	5.8	6.7	6.5	6.4	6	7	5.9	6.2	6.9	6.4	5.5	5.6	4.6	5.2	5.2	5.5	5	4.8	2.9
Tyr 57-OH (-)	-7.2	-5.4	-4.4	-4	-5.2	-4.8	-5.1	-5.5	-6	-6.5	-5.7	-5.7	-5.3	-5	-4.9	-3.9	-3.5	-3.4	-2.9
Tyr 57-OH (+)	5	4.7	4.8	3.9	3.4	4.2	5.2	4.9	3.9	3.7	4.7	5.3	5.3	4.9	4.4	4.1	3.2	2.7	2.8
W401(-)	-5.8	-5.8	-6.2	-5.6	-6.3	-6.9	-7	-6.9	-7.7	-7.4	-7.3	-8.2	-8.4	-9	-6.6	-5.7	-4.8	-5.2	-7.8
W401(+)	2.8	3.2	3.1	3.1	3.1	3	3.2	3.5	4	2.8	3.8	3.6	4.1	3.5	3.6	3.6	2.8	0	0
W400(-)	-5.1	-4.8	-4.2	-3.3	-3.8	-3.9	-5.7	-5.8	-6	-5.3	-4.8	-4.8	-4.1	-5.1	-5	-5.7	-5.4	-6.3	-6.2
W400(+)	3.6	3.3	0	2.9	3.1	3.5	3	3.1	4	3.6	3.3	3.8	3.8	4.4	3.6	3.7	2.6	2.6	0
W402(-)	-10.9	-10.4	-9.9	-9.6	-10	-10.7	-10.5	-10.1	-9.7	-8.5	-7.6	-8.9	-9.9	-10.5	-9.8	-9.1	-7.6	-6.7	-5.8
W402(+)	6.7	6.2	5.5	5.2	5.7	6.1	6.2	6	6.4	6.2	6.8	6.5	6.4	5.8	6	6.3	5.7	5.2	3.6
W403(-)	-2.8	-2.9	0	0	0	-3.1	-3.4	-3.8	-3.9	-3.4	-3.3	-4.3	-5.7	-5.3	-4.4	-4.4	-3.9	-3.5	-2.5
W403(+)	0	0	0	0	2.5	2.9	3.9	3.9	4.8	3.5	3	2.9	3.6	3.3	0	2.7	2.7	0	0
W404(-)	-2.8	-2.6	0	0	-2.6	-3	-3.3	0	-2.5	-2.7	-3.7	-3.7	-3.4	-3	-2.9	-3.1	-3.7	-3.7	-4.8
W404(+)	3	3	2.7	3	2.5	2.5	2.5	2.6	2.5	2.5	2.8	3.8	3.9	4.2	3.1	3	2.3	2.5	0
Within 4Å to RET																			
Pro186-Cβ (-)	-4.7	-4.1	-3.3	-3.2	-3.3	-3.9	-4.5	-3.9	-4	-3.6	-3.6	-4.1	-4	-4	-3.1	-3.2	0	0	-3.1
Pro186-Cβ (+)	0	0	2.5	3.6	3.2	3	3.1	4	3.7	3.3	2.8	3.4	3	3.4	3.7	2.9	2.9	3.6	2.9
Pro186-O (-)	-3.8	-3.4	-2.8	-2.7	-2.9	-3.6	-3.2	-3.6	-3.8	-4.8	-4.3	-3.2	-2.7	-2.5	-2.6	-3.4	-2.8	-2.9	-3.6
Pro186-O (+)	4.4	5	3.8	3.1	2.8	3.3	2.7	0	3.1	3.9	4.7	4.7	3.8	3.7	3.3	2.7	3.1	2.5	0
Pro186-Cδ-N (-)	-4.2	-4	-2.5	-2.6	-2.9	-4.6	-5.7	-5	-4.7	-4.9	-4.7	-5.8	-5.8	-5.8	-5.8	-4.2	-4.6	-2.9	-2.8
Pro186-Cδ-N (+)	0	0	0	0	3.2	2.8	4	3.1	3.7	4.7	4.9	4.3	4.1	3.8	2.7	0	0	0	0
Trp 182-Nε1 (-)	-5.4	-4.2	-3.7	-3	-3	-2.9	-3.7	-4	-3.8	-4.1	-4.7	-4.8	-5	-4.8	-4.7	-3.4	-3.3	-2.7	-3.7
Trp 182-Nε1 (+)	4.3	3.3	5.4	4.9	5.8	4.2	3.7	3	4.3	4	4.3	4.2	4	3.4	3.5	3.4	3.5	3.2	4.3
Trp 86-Nε1 (-)	-5	-4.4	-4.2	-4.2	-4	-4.6	-4.8	-4.5	-4.6	-4.1	-4.5	-4.5	-4.6	-4.3	-3.9	-3.1	-3.2	-2.7	-4.4
Trp 86-Nε1 (+)	3.3	2.7	3.4	4.1	4.5	4.1	3.8	3.4	2.5	2.5	2.5	2.5	0	2.8	2.9	3.5	2.6	3.8	3.5
Trp 86-Cε3(-)	-3.2	-4	-4.5	-4.9	-4.9	-5.6	-5	-4.2	-4.2	-4.4	-4.1	-4.2	-3.8	-4.7	-5.1	-4.6	-5.3	-4.3	-3.7
Trp 86-Cε3 (+)	2.7	2.6	3.4	3.7	4	3.8	3.7	3.7	3.7	4.1	4.5	3.8	3.6	3.1	3.2	3.2	3.2	3.1	3.2
Met 118-Sδ (-)	-5.6	-5.1	-4.8	-4.8	-5.1	-4.8	-5.4	-5	-5.3	-5.8	-6.2	-6.9	-6.4	-5.6	-5.9	-5	-5.6	-5	-5.4
Met 118-Sδ (+)	2.6	4.4	4.5	4.7	3.7	2.9	2.5	2.5	2.4	2.8	3.5	3.2	3	3.2	3.5	2.7	0	2.5	3.2
Ser 141 (-)	-3.7	-2.6	-2.6	-3.3	-3.8	-3.8	-3.9	-3.6	0	0	0	0	-2.5	-2.6	-3	-3.7	-2.8	-2.9	-3.5
Ser 141 (+)	3.3	3.8	3.6	2.9	2.5	3	3	0	0	0	0	3	2.5	3.4	4.1	3.1	0	0	0
Tyr 185-Cβ (-)	0	-3	-4.3	-3	-3.3	0	-2.9	-3.8	-4	-4.8	-5	-4	-2.8	0	-3.5	-3.5	-3.7	-3.3	-4
Tyr 185-Cβ (+)	4.2	3.4	3.2	2.6	3	0	0	2.7	3.9	4	3.8	3	3	0	2.7	2.6	2.6	0	3.9

Tyr 185-OH (-)	-3.7	-3.5	-3.8	-5.1	-5.6	-6	-6.3	-6.4	-6.3	-6.5	-6.3	-7.2	-7.6	-7.4	-6.8	-6.7	-5.2	-4.2	-4.1
Tyr 185-OH (+)	0	0	2.7	3.2	3.5	0	0	0	0	0	0	3.4	3.4	3	2.7	3.2	3.7	3	2.9
Met 145-Sδ (-)	-3.2	-2.7	-2.7	-3.4	-3.9	-5.1	-5	-5.1	-4.8	-4.4	-5.2	-5	-5.1	-5.6	-4.6	-4.6	-4.4	-5.5	-8
Met 145-Sδ (+)	0	0	2.8	0	0	0	0	0	0	0	0	2.7	2.7	3.9	4	4	4.1	4.1	6
Thr 89-Oγ1(+)	3.8	4.4	4.6	5.4	5.7	6	5.1	4	3.1	3.5	3.7	3.9	3.4	4	4.6	4.6	5.1	4.7	2.7
Thr 89-Cγ2(-)	0	0	0	0	0	-3	-3.9	-4.3	-3.2	-2.9	-2.7	-3.1	-3.9	-4	-4.7	-4.7	-3.6	-3.4	-3
Helix A																			
Met 20-Sδ (-)	-4	-3.9	-3.1	-3.3	-2.5	-2.5	-3.7	-5	-6.7	-6.4	-6.4	-5.9	-6.2	-6.4	-4	-4	-3.4	-5.8	-4.8
Met 20-Sδ (+)	0	0	0	0	0	2.8	3	2.7	2.8	3.3	3.1	3.8	3.2	2.7	3.4	3.4	4.8	5	5.2
Helix B																			
Thr 47-O(-)	0	0	0	0	0	-2.7	-3.5	-4	-3.7	-5.4	-6.2	-6.6	-5.9	-5.2	-3.8	-3.8	-2.8	-3.2	0
Thr 47-O(+)	0	0	0	0	0	0	3.2	4.2	5.2	5.4	5	4.7	5	4.9	3	2.8	2.5	2.9	0
Leu 48-O(-)	-2.7	-2.9	-4	-4.5	-5	-4.6	-4.7	-5.2	-5	-4.9	-3.6	-3.6	-4.3	-4.2	-3.6	-3.5	-3.6	-2.9	-3.1
Leu 48-O(+)	3.1	3.2	2.5	2.7	3.2	4.9	5	4.6	3.4	2.5	3.6	3.6	4.3	4.3	2.7	2.7	2.5	2.9	4.5
Val 49-O(+)	3.9	3.6	5.4	5.5	6.5	5.2	4.7	4.2	5.1	5.2	5.3	4.6	4.6	4.8	5	5	4.5	5	3
Pro 50-O-C-N(+)	3.8	3.6	5.3	5.5	6.6	5.2	4.8	4.1	5.1	5.2	5.3	4.6	4.4	4.8	5	5	4.6	5	3.9
Ala 51-C-O (-)	-4	-3.4	-3	-2.9	-3.6	-4	-4.7	-5	-5.4	-6	-6.1	-6.5	-5.9	-6.3	-4.5	-4.5	-4.3	-3.4	-2.6
Ile 52-O(+)	3	3.4	3.8	3.6	4.7	4.8	6	5.5	6.4	5.3	5.4	4.9	3.9	4.9	4.5	4.5	2.5	2.5	2.7
Ala 53-Cβ(-)	-3.4	-3.1	-3	-3.5	-3.4	-4.1	-3.4	-3.5	-3.3	-3.8	-3.9	-3.5	-3.1	-3.6	-5.1	-5.1	-5.3	-4.7	-3.8
Ala 53-Cβ(+)	0	0	0	0	0	3.2	0	3	3.1	3.1	3.9	4	4.7	3.9	3	3	3.3	2.6	4.2
Ala 53-O (-)	-4	-3.6	-3.1	-2.5	-2.5	-3.6	-4.2	-4.3	-3.9	-4.1	-4.7	-4.6	-4.5	-4.5	-2.6	-2.6	0	0	-3.4
Phe 54-C(-)	-2.7	-2.5	-3.1	-3	-4.5	-4.5	-5.6	-5.3	-4.7	-3.5	-4	-4	-3.9	-3	-3.4	-3.3	0	0	0
Met 56 (-)	-3	-3	-2.9	-3.4	-4	-6	-7.3	-7.2	-6.1	-5.8	-5.1	-6.1	-4.5	-4.7	-5.6	-5.5	-6.3	-6.4	-6.3
Met 56 (+)	3.6	3.8	4.3	3.2	3.5	4.5	5.3	4.8	4.6	5.6	5.2	5.4	5.1	5.5	4.4	4.4	4	3.7	2.8
Helix C																			
Ala 84-O(-)	-4.7	-4.5	-5.6	-4.9	-4.8	-5.5	-5.7	-5.7	-4	-3.6	-3.8	-4.7	-4	-3.5	-3.5	-3.4	-3.4	-3.1	-3.8
Phe 88-O(-)	-3.6	-2.8	-3.5	-2.9	-3.1	-4.6	-5.5	-6.3	-5	-5.4	-5.6	-6.4	-5.7	-4.6	-3.9	-3.8	-4.8	-3.6	-4.9
Helix F																			
Ser 183-O (-)	-4.6	-4.5	-4.1	-4.3	-4.3	-4.9	-5.1	-5.9	-5	-5.4	-4.4	-3.9	-4	-4.8	-4.2	-4.3	-4.1	-2.9	0
Ser 183-O (+)	0	0	3.5	2.9	2.8	2.9	3.2	3	3.4	4.1	3.7	3.7	3	3.5	4	4	3	2.5	2.5
Ala 184-O (-)	-3.6	-4.2	-3.2	-2.6	0	0	-3.4	-3.9	-4.4	-4.4	-4.4	-4.4	-4	-3.6	-2.9	0	0	0	-3.2
Helix G																			
Leu 206-C(+)	0	0	0	0	3.7	3.1	3.6	4.3	4.4	4.3	4.4	4.9	3.9	3.6	2.9	2.9	0	0	0
Leu 207-C-N(-)	-3.5	-3.6	-3	-3.2	-2.7	-3.1	-3.3	-4.3	-4.4	-4.6	-4.6	-3.9	-3.8	-4.6	-3.3	-3.3	0	0	0
Leu 207-C-N(+)	4.9	4.9	3.8	3.5	3.6	3.6	3.6	4.2	4.5	5	5.3	3.8	4.1	3.6	2.9	3.6	0	0	0
Phe 208-O(-)	-4.2	-5	-4.6	-4.4	-3.7	-4.7	-5	-4.9	-4.5	-4.5	-4.5	-4.5	-4.4	-4.8	-4.7	-4.7	-4.5	-4.6	-3.7
Phe 208-O(+)	4.1	4.2	3.7	0	0	3.6	3.6	4.7	5	4.9	5.2	5.4	4.5	0	0	0	0	0	0
Met 209 (-)	0	0	0	-2.7	-2.5	-2.8	-3.6	-2.8	-2.6	-3.3	-3	-4	0	0	-3.7	-3.7	-3.8	-3.4	-2.9
Val 210 (-)	0	0	0	0	0	-2.7	-4	-3.7	-3.1	-3.1	-3.3	-4	-4.2	-3.5	0	0	0	0	-2.6

Supporting Data File 1: Table of the amplitudes of the difference Fourier electron density map (F_{obs}^{light} - F_{obs}^{dark}) changes of key residues and key water molecules with time.

Supplementary Movies:

Movie S1: Long distance view of the evolution of difference Fourier electron density (F_{obs}^{light} - F_{obs}^{dark} contoured at 4.0 σ, golden negative, blue positive) with time.

Movie S2: Evolution of difference Fourier electron density (F_{obs}^{light} - F_{obs}^{dark} contoured at 4.0 σ, golden negative, blue positive) along the retinal chromophore.

Movie S3: View of the electron density changes (F_{obs}^{light} - F_{obs}^{dark} contoured at 4.0 σ, golden negative, blue positive) along the counter-ion hydrogen bonding network.